BROWN UNIVERSITY

Solute strengthening from first-principles and applications to Al and Mg alloys

by

Gerard Paul Marcelo Leyson

A dissertation submitted in partial fulfillment for the degree of Doctor of Philosophy

in

Solid Mechanics

School of Engineering

May 2013

This dissertation by Gerard Paul M. Leyson is accepted in its present form

by the School of Engineering as satisfying the

dissertation requirement for the degree of Doctor of Philosophy.

Date _____ _____

William A. Curtin, Director

Recommended to the Graduate Council

Date _____ _____

Allan F. Bower, Reader

Date _____ _____

Pradeep Guduru, Reader

Date _____ _____

Sharvan K. Kumar, Reader

Approved by the Graduate Council

Date _____ _____

Peter M. Weber, Dean of the Graduate School

Vitæ

Gerard Paul Marcelo Leyson was born on March 1, 1981 in the Marikina, Philippines. In 2001, he was awarded the Singapore Ministry of Foreign Affairs ASEAN[1] scholarship and took an undergraduate degree in the National University of Singapore (NUS) in Materials Science. In that program, he finished with First Class Honours in 2005 and was awarded the Materials Research Society (Singapore) and the Lijen Industrial Development medals. From there, he pursued a Masters Degree in the same university under supervision of Prof. Chiu Cheng Hsin and graduated in 2007. He is currently pursuing a doctoral degree in Solid Mechanics at Brown University under the guidance of Prof. William A. Curtin. In September 2011, he came to Ê cole Polytechnique Fédéral de Lausanne (EPFL) in Switzerland as a visiting doctural student in the Institute of Mechanical Engineering.

[1] Association of South East Asian Nations

"Every honest researcher I know admits he's just a professional amateur. He's doing whatever he's doing for the first time. That makes him an amateur. He has sense enough to know that he's going to have a lot of trouble, so that makes him a professional."

Charles Franklin Kettering (1876-1958) U. S. engineer and inventor.

Abstract of "Solute strengthening from first-principles and applications to Al and Mg alloys"

by Gerard Paul Leyson, Ph.D, Brown University, May 2013

In this dissertation, a quantitative, parameter free model to predict the flow stress as a function of temperature and strain rate of such alloys is presented. The model builds on analytic concepts developed by Labusch but introduces key innovations rectifying shortcomings of previous models. To accurately describe the solute/dislocation interaction energies in and around the dislocation core, density functional theory and a flexible-boundary-condition method are used. The model then predicts the zero temperature flow stress, the energy barrier for dislocation motion, and thus the finite temperature flow stresses. The model is first used to predict the flow stresses of various Al alloys. Excellent results are obtained for Al-Mg and Al-Mn. Al-Fe with ppm levels of Fe is not predicted well but, using experimental results for Fe, results for the quasi-binary Al-Cr-(Fe) and Al-Cu-(Fe) alloys agree well with experiments. The model is also consistent with the "stress equivalency" postulate of Basinski. The model is then applied to Mg-Al alloys undergoing basal slip. Due to the wide partial separation of the Mg basal edge dislocation, a smaller roughening is required to decorrelate the solute fluctuations in the partials compared to that required to decorrelate the fluctuations in the "far field". As a consequence, the dislocation has two stable configurations. When these two configurations are taken into account, the model predictions are in good agreement with experiments over a wide range of solute concentrations and temperature. The model also explains the origins of the "plateau stress" observed in experiments. Finally, the model in conjunction with the standard Friedel strengthening model is used to study the transition between weak-pinning and strong-pinning at finite temperatures. The transition concentration is found to be a strong function of the dislocation core structure and can be significantly different from the zero-temperature transition concentration. It is also found that, for the case of Al-X and basal Mg-Al alloys, the weak-pinning mechanism is always dominant at temperatures and concentrations relevant to engineering applications.

Acknowledgements

First and foremost, I would like to express my heartfelt thanks to Prof. William A. Curtin. I am lucky that I have worked with a supervisor that is concerned both with the quality of the research as well as the personal growth of his students. His guidance over the past few years have been invaluable and I will always be grateful that I have had this opportunity to work with him.

I would also like to thank General Motors for supporting my research, with special mention to Dr. Lou Hector Jr. At the dawn of my PhD studies, Dr. Hector took me under his wings and showed me the wonders of first-principles calculations.

I would like to thank everyone who has helped me get to where I am today. One should not forget his roots lest he lost himself in the future. A special thanks to my parents, who have been a constant source of support and encouragement. I would also like to mention Prof. Augusto Hemorsilla, who is one of the major reasons I pursued a career in the Academia. It has been a long time, but I have not forgotten all you have taught me.

Finally, I would thank my friends, near and far. I apologize for the general statement, but unfortunately, you are too numerous list here. That said, I'm sure you know who you are. Thank you for keeping me sane all these years.

Contents

List of Figures

List of Tables

Chapter 1

Introduction

Five thousand years ago, Sn and Cu were mixed to form Bronze, ushering in a new era for mankind. Since that time, alchemists and scientists have developed many more materials through alloying of base metals. The results of their efforts surround us today in the form of cars, computer chips, airplanes, jet engines, and hip implants, that use advanced engineered materials ranging from lightweight Magnesium alloys to high-strength, high-temperature Ni-based superalloys. The evolution in material design has been achieved through a combination of experiment, physical insight based on mechanistic ideas, and modeling of those mechanisms to verify basic concepts and scaling. In recent years, computational materials science has emerged as a powerful supplement to experiments, providing guidelines for materials development and supporting trends found experimentally. However, quantitative parameter-free computational prediction of material properties has yet to be achieved for properties as basic as the flow or yield stress in metals.

In this dissertation, we present a new approach for quantitative prediction of metal yield stress in solute-strengthened materials, with application to Aluminum (Al) and Magnesium (Mg) alloys. Solute-strengthening arises in Al 2XXX, 3XXXX, 5XXX and 6XXX alloys, which represent important classes of lightweight alloys where solute strengthening is crucial and for which an understanding of strengthening via multiple types of solutes is valuable for green engineering/recycling. Magnesium alloys, with excellent material properties such as low density and high specific strength, have been enjoying increased interest in the recent years for similar reasons. However, wide-spread adoption of Mg alloys is held back by limitations in formability in these alloys. It is therefore important to develop theoretical and computational tools to gain insight in the strengthening mechanisms in these alloys and guide their development. Although applied specifically to Al and Mg alloys, the framework developed here is quite general and is applicable to other fcc metals, other solute atoms, and also various other systems such as basal slip in hcp alloys such as Ti and Zn.

It has been long known that alloys containing substitutional solutes exhibit strengths higher than that of pure metals. Solutes interact with the dislocations and pin them in place so that a higher stress must be applied in order to overcome the solute pinning. The underlying physics is associated with the fact that, due to lattice mismatch, a substitutional solute acts as an eigenstrain that interacts with the stress field created by the dislocation. The interaction energy between a dislocation at $\vec{r} = 0$ and a solute at $\vec{r}$ is given by

$$U\left(\vec{r}\right) = \int_{\Omega} \sigma_{ij}\left(\vec{r'}\right) \epsilon^{s}_{ij}\left(\vec{r'} - \vec{r}\right) d\vec{r'} \tag{1.1}$$

where $\sigma_{ij}(\vec{r'})$ is the stress field at $\vec{r'}$ due to the dislocation and $\epsilon^{s}_{ij}(\vec{r'} - \vec{r})$ is the strain

field at $\vec{r'}$ due to the solute. If the solute is approximated as a point dilitational source, then $\epsilon^s_{ij}(\vec{r'} - \vec{r}) = \Delta v_m \ \delta(\vec{r} - \vec{r'})$ and the solute-dislocation energy can be approximated by

$$U\left(\vec{r}\right) \approx -p\left(\vec{r}\right) \Delta v_m \tag{1.2}$$

where Δv_m is the misfit volume of the solute and $p = -\sigma_{kk}/3$ is the pressure field exerted by the dislocation at the location of the solute [7]. In other words, the energy is equal to the work required to insert a dilatational source of strength Δv_m against the dislocation pressure field. At finite concentrations, the solutes can modify the elastic modulus of the material and generate a second-order contribution to the energy [7]. Since the dislocation pressure field decreases as $1/r$, there is a gradient in the interaction energy that ultimately leads to dislocation pinning phenomena.

Solute strengthening is typically divided into two classes: strong-pinning and weak-pinning. These two classes gives rise to different scaling of the strengthening with concentration as well as different energy and length scales.

1.1 Strong-pinning mechanism

In the case of strong-pinning, individual solutes pin the dislocation at the solute position. Applying a stress τ causes the dislocation to bow out between these pinning points with an angle θ, exerting a force $\vec{f} = -\nabla_{\vec{r}} U\left(\vec{r}\right)$ on the pinned portion of the dislocation (schematically shown in Figure 1.1(a). Friedel pioneered the solution to this problem [8]

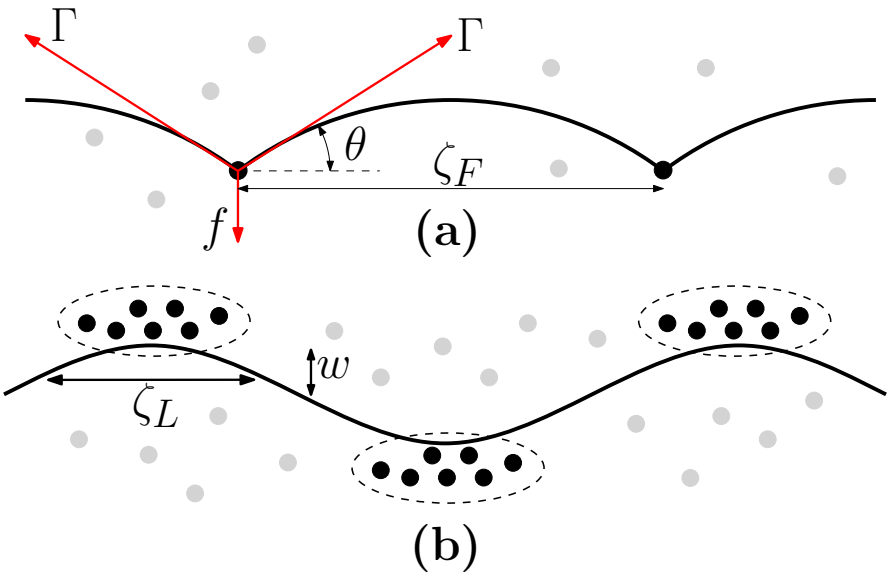

FIGURE 1.1: A schematic representation of (a) the Friedel strengthening mechanism, wherein solutes are treated as point pinning obstacles, and (b) the Labusch strengthening mechanism, wherein favorable fluctuations in solute concentration trap the dislocation segments.

and a short summary of his results are presented here. Once force equilibrium is established, the line tension Γ balances out $f = |\vec{f}|$,

$$f = 2\Gamma \sin\theta. \tag{1.3}$$

For small concentrations, the resistive force can also be expressed as

$$f = \tau b \zeta_F \tag{1.4}$$

where ζ_F is the average distance between obstacles in the dislocation line. When τ is under but close to the flow condition, the length of the pinned segments on average follows "Friedel sampling",

$$\frac{\zeta_F(\tau)}{\lambda} = \left(\frac{2\Gamma}{\tau b \lambda}\right)^{\frac{1}{3}} \tag{1.5}$$

where $\lambda \sim c^{-1/2}$ is the average solute spacing on the slip plane and b is the Burgers vector. The zero temperature yield stress for the Friedel mechanism, τ_{y0}^{F}, then corresponds to the stress required to overcome the maximum resistive force f_{max}. Combining Eqns. (1.3)–(1.5), yields an expression for τ_{y0}^{F},

$$\tau_{y0}^{F} = \frac{f_{max}}{b\zeta_L\left(\tau_{y0}^{F}\right)} = \left(\frac{f_{max}}{2\Gamma}\right)^{\frac{3}{2}}\left(\frac{2\Gamma}{b^2}\right)c^{\frac{1}{2}}. \tag{1.6}$$

There have been refinements to the strong-pinning model [7, 9], but the general scaling behavior of the yield strength with concentration is identical for all strong-pinning models.

1.2 Weak-pinning mechanism

Weak pinning solutes trap the dislocation in regions where the collective configuration of the solutes are relatively energetically favorable for the dislocation. Because of random fluctuations in solute concentration, any given segment of the dislocation may be able to lower its energy by bowing out toward nearby favorable solute configurations at the cost of increased elastic energy due to the bowing, shown schematically in Figure 1.1(b).

For clarity, the discussion on this section follows Zaiser's presentation of Labusch's analysis [10]. For a more detailed treatment of the derivations, readers are directed to this reference. The total energy of the dislocation is given by

$$E_{tot} = E_p + E_{el} \tag{1.7}$$

where E_p is the energy gain due to favorable solute fluctuations and E_{el} is the energy cost due to bowing out. In this treatment, the solute/dislocation interaction energy is assumed to have the form of $U_{max} f(\vec{r})$, where $f(\vec{r})$ is a non-dimensional function with a finite range w[1]. Considering a dislocation segment of length X, the segment must at least bow out a distance w in order to take advantage of favorable solute fluctuations. The change in elastic energy is then given by

$$\Delta E_{el} = \left(\frac{\Gamma}{2}\right)\left(\frac{w}{X^2}\right) X. \tag{1.8}$$

The potential energy change, on the other hand, is proportional to the fluctuation of the number of solutes $\partial n = \sqrt{cw^2 X/b^3}$ within the interaction volume Xw^2,

$$\Delta E_p = -U_{max}\partial n = U_{max} w\sqrt{cX/b^3}. \tag{1.9}$$

When X is small, the cost of bowing ΔE_{el} is greater than the energy gain ΔE_p due to fluctuations. Therefore, there is a critical lengthscale ζ_L (referred to as the "Labusch length") at which bowing out becomes favorable and the dislocation is free to adjust to the energy landscape. This critical lengthscale is obtained by substituting Eqns. (1.8) and (1.9) into Eqn. (1.7), then setting E_{tot} to zero,

$$\zeta_L \approx \left(\frac{\Gamma^2 w^2}{4U_{max}^2 c}\right)^{\frac{1}{3}} b. \tag{1.10}$$

[1] Specifically, $f(0) = 1$ and $\int_{-\infty}^{\infty} f(\vec{r})\, d\vec{r} = w^3$

The characteristic energy scale E_L associated with a "Labusch length" is then given by

$$E_L = \left(\frac{\Gamma w^4 U_{max}^2 c}{2b^3} \right)^{\frac{1}{3}} \tag{1.11}$$

and the zero temperature flow stress τ_{y0}^L follows as

$$\tau_{y0}^L = \frac{E_L}{bw\zeta_L} = \left(\frac{c^2 U_{max}^4}{w\Gamma b^9} \right)^{\frac{1}{3}}. \tag{1.12}$$

Regardless of the mechanism, the degree of strengthening is a function of solute concentration c, some measure of the magnitude and/or gradient of the solute-dislocation interaction energies $U(\vec{r})$, the dislocation line tension Γ, the solute misfit volume Δv_m, the Burgers vector b, and shear modulus μ of the matrix. These mechanisms have been characterized in classical studies [9, 11–14]. Solutes that exhibit strong pinning are said to follow "Friedel statistics" with a yield stress that exhibits a concentration dependence of $c^{1/2}$, while weak pinning solute follow "Mott statistics" and a yield stress scaling as $c^{2/3}$.

1.3 Transition between strong- and weak-pinning regimes

The transition between strong and weak pinning regimes has also been studied by Labusch [13, 15]. Labusch quoted the paramater,

$$\beta = \frac{f_{max} b^2}{4\Gamma c w^2} \tag{1.13}$$

which determines determines the dominant pinning mechanism of the material. Specifically, if $\beta \gg 1$ then the strong-pinning mechanism dominates and if $\beta \ll 1$, weak pinning dominates [2]. Equation (1.13) is can be derived by taking the ratio between the zero-temperature yield stresses of the Friedel and the Labusch strengths (given by Eqns. (1.6) and (1.12) respectively), and therefore is inherently a zero-temperature quantity. Regardless, this parameter is widely quoted in the literature [16–19] and is routinely applied to interpret finite-temperature data. The behavior of the strong-/weak-pinning transition with temperature has not been studied in the literature.

1.4 Yield strength at finite temperature

At finite temperatures, the dislocation can be thermally activated over an energy barrier it encounters at stress less than the zero-temperature yield stress. Derivation of the finite temperature yield stress $\tau_y(T)$ can be obtained through thermal activation theory [20, 21]. For concreteness, the $\tau_y(T)$ of a dislocation experiencing strong-pinning is derived in this section. The dislocation is assumed to have a quadratic-cubic energy landscape characterized by a maximum resistive force f_{max} and energy barrier E_{max}. A resolved shear stress τ lowers the energy barrier by $\tau b \zeta_F x$. The energy landscape of the dislocation with stress is therefore given by

$$E(x) = E_{max}\left[3\left(\frac{x}{d}\right)^2 - 2\left(\frac{x}{d}\right)^3\right] - \tau b \zeta_F(\tau)\, x \tag{1.14}$$

[2] The transition parameter given in Eqn. (1.13) is essentially the same β parameter was first quoted in Ref. [13], although derived through a different approach. However, in that paper, Labusch clearly states that his theory is valid when $\beta \gg 1$. Despite this inconsistency, subsequent referral to this β parameter takes the weak-pinning mechanism to be applicable when $\beta \ll 1$.

where $d = \frac{3}{2}E_{max}/f_{max}$. The stress dependent energy barrier $\Delta E(\tau)$ is obtained by taking the difference between the two critical points in Eqn. (1.14). Using Eqn. (1.6) and the fact that $\zeta_F(\tau)/\zeta_F\left(\tau_{y0}^F\right) = \left(\tau/\tau_{y0}^F\right)^{\frac{1}{3}}$, $\Delta E(\tau)$ can be expressed as

$$\Delta E(\tau) = E_{max}\left[1 - \left(\frac{\tau}{\tau_{y0}^F}\right)^{\frac{2}{3}}\right]^{\frac{3}{2}}. \tag{1.15}$$

For a quasistatic loading, such that the system is always in a state of metastable equilibrium, the rate of escape ν by activation over the stress-dependent barrier height $\Delta E(\tau)$ can be approximated using transition state theory [21] as

$$\nu = \nu_\circ \exp\left(-\frac{\Delta E(\tau)}{kT}\right) \tag{1.16}$$

where $\nu_\circ$ is the attempt frequency, k is the Boltzmann constant and T is the temperature. The microscopic dislocation escape rate ν can be related to the macroscopic strain rate by the well established model [12],

$$\dot{\epsilon} = \dot{\epsilon}_\circ \exp\left(-\frac{\Delta E(\tau)}{kT}\right), \tag{1.17}$$

where $\dot{\epsilon}_\circ = \rho b d \nu_\circ$, ρ is the dislocation density per unit area and d is the flight distance over which the dislocation moves after each escape. Equations (1.17) and (1.15) can be inverted to obtain the finite temperature stress required for dislocation flow as

$$\tau_y(T) = \tau_{y0}^F\left[1 - \left(\frac{kT}{E_{max}}\ln\frac{\dot{\epsilon}_\circ}{\dot{\epsilon}}\right)^{\frac{2}{3}}\right]^{\frac{3}{2}}. \tag{1.18}$$

The procedure is quite general and can be applied straightforwardly to the weak-pinning model as well as other energy landscapes. In general, the stress dependent energy barrier can be approximated by [20]

$$\Delta E\left(\tau\right) = \Delta E_{\circ}\left[1 - \left(\frac{\tau}{\tau_{y0}}\right)^{p}\right]^{q} \tag{1.19}$$

where $\Delta E_{\circ}$ is the characteristic energy barrier for the strengthening mechanism, $0 < p \leq 1$ and $1 < q \leq 2$. For strong-pinning, $p = 2/3$ while for weak-pinning, $p = 1$. The exponent q depends on the force/energy profile assumed. The corresponding finite temperature yield stress takes the general form,

$$\tau_{y}\left(T\right) = \tau_{y0}\left[1 - \left(\frac{kT}{\Delta E_{\circ}}\ln\frac{\dot{\epsilon}_{\circ}}{\dot{\epsilon}}\right)^{\frac{1}{q}}\right]^{\frac{1}{p}}. \tag{1.20}$$

1.5 Limitations of existing models

Both strong and weak pinning models, as presented in the existing literature, have features that are ill-defined, inhibiting predictability. For strong pinning, only the solutes along the glide plane are usually considered even though the interaction energies of solutes off the glide plane can remain substantial in the vicinity of the dislocation. Applicability of the point pinning model at concentrations typical of engineering alloys (on the order of 1%) is questionable because (i) the distance between point pinning solutes, even just in the glide plane, is only a few Burgers vectors and (ii) for fcc and some hcp metals, wherein the dislocation core is split into partials that are separated by a nanometer or more, multiple solutes can be interacting with the dislocation in the

same region. Furthermore, the total interaction energy U_{tot} of a dislocation line of length L lying along the z-direction is the sum of all individual solute/dislocation interactions. Since solutes with the same x- and y-coordinates have the same interaction energy, U_{tot} is given by

$$U_{tot} = \sum_{ij} n_{ij} U\left(x_i, y_j\right) \tag{1.21}$$

where n_{ij} is the number of solutes with position (x_i, y_j) perpendicular to the dislocation line. For random alloys, and for the $1/r$ scaling of the energy with distance, the total energy can be divergent (although angular terms can lead to cancellation). The mean interaction energy of a dislocation in a random distribution of solutes is

$$\langle U_{tot} \rangle = \sum_{ij} \langle n_{ij} \rangle U\left(x_i, y_j\right) = cN \sum_{ij} U\left(x_i, y_j\right) \tag{1.22}$$

where c is the concentration of the solute and N is the number of atomic sites along the dislocation line. The mean energy $\langle U_{tot} \rangle$ is thus independent of dislocation position as the dislocation moves from one atomic position to the next equivalent one. The finite-difference measure of the configurational glide force $f_c = -\partial \langle U_{tot} \rangle / \partial x$ due to the mean effect of the solutes,

$$f_c = \frac{2cN}{b} \sum_{ij} \left[U\left(x_i - \frac{b}{2}, y_j\right) - U\left(x_i, y_j\right) \right] \tag{1.23}$$

is then zero. Therefore, it is only the random *fluctuations* in solute concentration around the dislocation that can provide strengthening, and this is the genesis of the weak-pinning models. Segments along an initially straight dislocation can be attracted to energetically-favorable fluctuations, and bow out towards them, at the cost of dislocation

line energy, as discussed in the pioneering work of Labusch [13, 15]. Difficulties arise, however, because the scaling of the energy fluctuations is proportional to $(p\Delta v_m)^2$, thus depending on distance as r^{-2}, for which the summation over all solutes still diverges as $\ln(R)$ where R is the system size. To circumvent this problem, previous works have either arbitrarily set a finite interaction range or considered only solutes along the glide plane. Predictions of such models depend on the *ad-hoc* finite range of the interactions, which is typically taken to be on the order of b. Hence, no insight yet exists into selecting any "correct" range or its possible dependence on alloy type or other material parameters. As noted above, neglect of solutes outside the glide plane is also not justified. Finally, none of the literature models accounts for solute interactions with the actual dislocation core structure.

1.6 Numerical simulations of solute-strengthening

Computer simulations based on continuum analysis [22–25] have been developed to better understand the strengthening behavior of solute strengthened alloys. In these studies, the dislocation is modeled as a continuum line defect and often only the interactions between the dislocation and solutes in the glide plane are considered. While providing insight into more-detailed behavior of the dislocations, such as temperature effects and dynamics of dislocation motion, these approaches have inherent limitations comparable to those associated with the corresponding analytic models. To address some of these limitations, molecular dynamics methods have recently been used to better describe the physics occurring in the core region [26–31] while also capturing the effects of solutes off the glide plane, and permitting some assessment of energy barriers to dislocation motion

[26]. It is difficult, however, to capture the proper mesoscale dislocation configurations on the 10-100nm scale via MD. MD studies are also limited to systems where the semi-empirical interatomic potentials for the alloy constituents are well-established. Even then, such potentials are often not designed to capture solute/dislocation interactions and can give inaccurate predictions[32]. Recent advances in computational capabilities have enabled the use of first-principles calculations based upon Density Functional Theory (DFT) to capture both the mechanical and chemical processes occurring in the dislocation core [4, 33–35], providing improved input parameters for use in some existing models. For instance, Yasi *et al.* [4] used a point-pinning model in order to predict basal-slip strengthening for various solutes in magnesium alloys and the predicted zero temperature strength of magnesium alloys compared favorably with experiments. Zander *et al.* [34, 35] used first-principles calculations to determine the size and modulus misfit parameters of solutes in aluminum alloys and used this information in conjunction with the Labusch (weak-pinning) model to develop a one-parameter strengthening model.

1.7 Overview of the dissertation

Despite of all the excellent progress made in this field, existing models are either non-quantitative, rely on fitting with existing experimental data or make predictions at zero-temperature. There is, therefore, a need for a robust and quantitative theory that predicts finite temperature yield behavior of arbitrary substitutional alloys.

This dissertation is organized as follows. In Chapter 2, we develop a new weak-pinning theory that addresses the limitations of existing models and apply it to Al-X alloys (X = Mg, Si, Cu, Cr, Mn and Fe). The new theory is parameter-free and takes input from first-principles calculations. As a result, the model gives quantitative predictions of finite temperature yield stresses directly from first-principles. We make predictions to several alloys cited in the literature and assess the accuracy of the predictions. In Chapter 3, we apply the theory to Mg-Al alloys without modification. As with previous chapter, predictions of the finite temperature yield stresses are compared to experimental data available in the literature. In Chapter 4, we explore the transition between the strong-pinning and the weak-pinning regime at finite temperature. A parametric study is conducted to see how the dislocation core structure affects the transition. The transition is also studied using existing first-principles data. Finally, we conclude our findings in Chapter 5.

Chapter 2

Solute strengthening in Al alloys from first-principles

2.1 Introduction

To facilitate the development of advanced materials, computational materials science can be used to create guidelines for design as well as give physical insight to experimentally-derived trends. However, robust and predictive models are critical. Predictions of the macroscopic mechanical properties, such as flow stress, work hardening, and fatigue behavior, in metals or other materials undergoing dislocation-mediated plastic flow, hold particular challenges because the behavior is controlled by interacting phenomena at multiple scales, from atomistic through mesoscale and microstructural scales, and is associated with the collective interactions among defects (solutes, dislocations, grain

boundaries, precipitates). In this chapter, we consider the problem of solute strengthening, which combines the chemistry of solute interactions with dislocations in the host metal and the resulting configurations of the dislocation line. The fundamental interactions are at the Angstrom scale, but other characteristic scales from 10–100 nm control the overall material response. By capturing the phenomena at these scales, the model here provides a robust means for predicting the yield stress of solute-strengthened alloys, here with application to Al alloys, as a function of composition, temperature, and strain rate.

Some basic aspects of solute strengthening mechanisms were established decades ago [11–14, 36]. The general picture is that substitutional solute atoms interact with dislocations due to their misfit volume and elastic mismatch, leading to pinning of the dislocations and thus requiring higher applied stresses to move the dislocations. The standard models assume the applicability of elasticity theory, treat the dislocation core as a point, neglect the solute atoms nearest to the core, and ignore divergences in the total solute/dislocation interaction energy [21]. While trends such as the scaling of the strengthening with solute concentration and the temperature dependence of the strengthening have emerged from some models [11–14, 36], they are not quantitatively accurate. For instance, Argon reports a factor of 4 difference in model predictions and experiments for the zero-temperature strengths of Al and Au solutes in Cu, with no estimate of the energy barriers for motion. Here, we capture both elastic and chemical contributions to the dislocation/solute interaction energies, show that the solute atoms nearest the (dissociated) core of a dislocation provide the largest contribution to the strengthening, and predict the energy barriers for motion and finite-temperature flow stresses, with

no adjustable parameters. The theory is also applicable to multi-component systems of dilute non-interacting solutes.

In this chapter, we expound on a model first presented in Ref. [37] which addresses both the divergence of the fluctuations in the interaction energy and the interaction energy for solutes within the core of the dislocation for arbitrary solute additions to aluminum. The latter is addressed using DFT to compute the interaction energy of solutes in the immediate region of a core, the geometry of which is also computed fully within DFT using a flexible boundary condition method. The former is addressed by following the general strategy of the Labusch model but with a careful analysis of the concentration fluctuations that considers the *spatial correlations* in those fluctuations, which then leads to a parameter-free theory with no divergences and no ad-hoc restriction on the range of solute/dislocation interactions. The resulting theory is applied to edge dislocations in Al-X alloys (X = Mg, Si, Cu, Cr, Mn and Fe) to predict the finite-temperature yield stress. Screw dislocations can be evaluated similarly, but the interactions are limited to the immediate core due to the absence of a pressure field around the screw dislocation, and so we consider the behavior of the edge dislocations to control the flow stress. The predictions for binary alloys Al-Mg and Al-Mn are in very good agreement with experiments over a range of concentrations and temperature. The model is not accurate for Al containing very dilute (ppm) Fe. When the anomalous behavior associated with very dilute concentrations of Fe is included, the predictions for Al-Cr-(Fe) and Al-Cu-(Fe) are also in very good agreement with experiment. Predictions of the activation volume, a sensitive test of the thermal activation process, are also in general agreement with experiments and the overall model obeys Basinski's "stress equivalency" principle.

Although the analysis is carried out using Al as the host matrix, the approach is applicable to other metals with substitutional solutes, particularly fcc and hcp systems. The predictive success of the model demonstrates that computational materials science can provide quantitative predictions of material mechanical behavior including the effects of alloying, opening the path to computational alloy design.

2.2 Computational Methods

Central to the solute strengthening mechanism is the interaction energy $U(\vec{r})$ between a solute at $\vec{r}$ and the dislocation structure centered at the origin $\vec{r} = 0$. In order to make quantitative predictions, it is necessary to accurately determine these interactions over a wide range of solute atoms and for all possible solute locations. In particular, solutes that are immediately above and below the partial dislocations and stacking fault (hereafter called "the core") are in a local environment much different from the bulk and therefore likely cannot be described by classical continuum elasticity. To accurately calculate the interaction energies of solutes in the core requires the use of a first-principles method to determine both the structure of the core and the energy changes when a solute atom substitutes for a host atom in the core region. Here, we use Density Functional Theory (DFT), implemented using the *Vienna Ab-initio Simulation Package* (VASP) [38, 39], Vanderbilt ultrasoft pseudopotentials [40], and the generalized gradient correction by Perdew and Wang [41, 42]. For bulk fcc Al, the method predicts a Burgers vector $b = 2.86$ Å, a shear modulus $\mu = 27.4$ GPa and a stacking fault energy $\sigma_{\mathrm{sf}} = 124$ mJ m^{-2}, all in good agreement with experiments [43]. The pseudopotential valence configurations and plane wave cutoff energies used for Al and for all of the substitutional solutes considered

here are summarized in Table 2.1. In calculating the relaxed core structure, a $2 \times 2 \times 8$ Monkhorst-Pack kmesh [44] and Methfessel-Paxton energy broadening [45] of 1 eV are used.

TABLE 2.1: Pseudopotential valence configurations (USPP = ultrasoft pseudopotential) and plane wave cutoff energies (PWCO) for atoms considered in this work.

Solute	USPP	PWCO (eV)
Al	$[Ne]3s^2 3p^1$	129
Cr	$[Ar]d^5 s^1$	227
Cu	$([Ar]3d^{10})p^1$	234
Fe	$[Ar]d^7 s^1$	238
Mg	$[Ne]3s^2$	106
Mn	$[Ar]d^6 4s^1$	295
Si	$[Ne]3s^2 3p^2$	151

We first determine the equilibrium geometry of a pure Al $a/2\,\langle 110\rangle$ edge dislocation with line direction along the $\langle 1\bar{1}2\rangle$ direction. We use the Lattice Green's Function method of Woodward *et al.* [43, 46]. In this method, a central group of ions (region I) containing the core are allowed to relax fully in response to DFT forces. The forces caused on a surrounding group of ions (region II) are then relaxed by updating ion positions in regions I and II using the Lattice Green's Function for a perfect infinite fcc crystal, and updating ion positions in an outer group of ions (region III) using the Continuum Elastic Green's Functions. The entire collection of ions and their valence electrons are surrounded by a small layer of vacuum within a periodic rectangular simulation cell. Region III serves to isolate the inner two regions from spurious electronic effects emanating from the surrounding vacuum region. This overall approach accommodates the long-range elastic fields of the dislocation, eliminating boundary effects that can plague standard approaches. Details of the method are found in the literature and are not repeated here. Here, we use a computational cell comprised of 569 Al ions forming

a prolate ellipse with major and minor axes dimensions of approximately 18 Å and 14 Å within an overall simulation box of dimensions 61Å×65Å×4.95Å and having periodic boundary conditions. Geometry optimizations were conducted until the forces on the ions in region I were 5 meV/Å or less. This ellipsoidal shape differs from the cylindrical shape used in Ref. [43] and provides more freedom for the splitting of the fcc core, and thus a better representation of the core structure than in the previous work. There are 50 ions in region I, 157 ions in region II, and 362 in region III. Nye tensor plots of the distribution of edge and screw components of the Burgers vector in the resulting relaxed dislocation core are shown in Figure 2.1. The equilibrium dislocation geometry shows that the core dissociates into Shockley partials separated by approximately 10.8 Å, well within the 50-ion region I, and slightly larger than the value previously quoted in Ref. [43].

The solute-dislocation interaction energy as a function of solute position is computed by substituting a single solute atom into each of 22 distinct atomic core sites immediately above and below the slip plane. For Mn and Fe solutes, only 9 distinct sites around one partial were used and the symmetry of the core was then invoked to obtain the energies around the second partial, an approach validated by the results obtained on other solutes using the entire set of 22 distinct sites. For Mg and Cr, two additional sites in the middle of the core in the second rows above and below the slip plane were also investigated. The structure was then relaxed using DFT-derived forces in region I until the forces on all the ions in region I were 5 meV/Å or less. The Lattice Green Function optimization was not performed because continuum elasticity and molecular statics using embedded atom method (EAM) potentials for Al-Mg show that the difference in energies is negligible

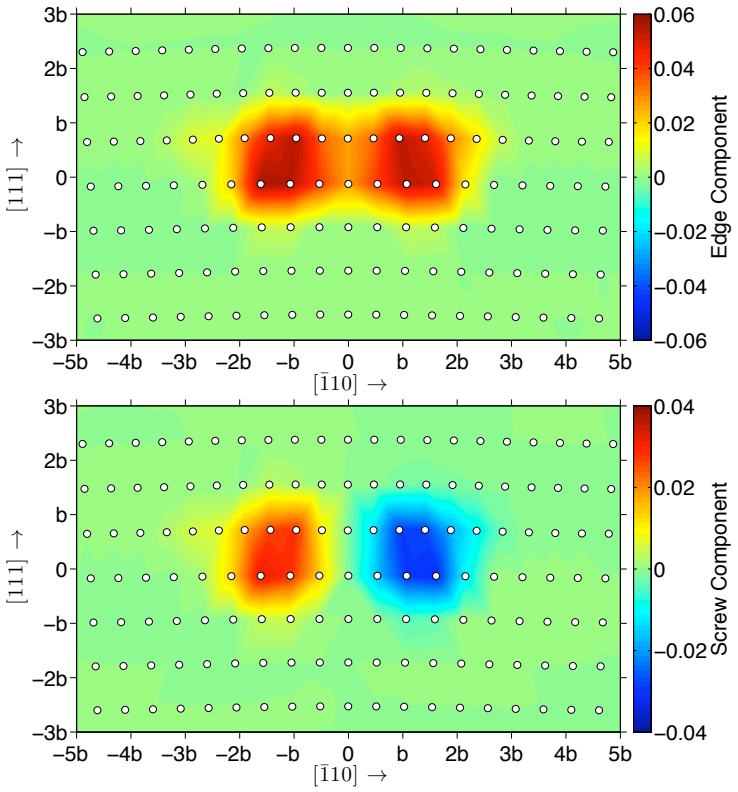

FIGURE 2.1: Nye tensor for the (a) edge and (b) screw components of the dislocation core computed using DFT and the Lattice Green's Function method. The x-axis is in units of Burgers vector. Peaks in the Nye tensor roughly correspond to the locations of the partial dislocations in the dissociated core.

($\sim$ 1 meV) when the radius of region I is much larger than the atomic radius, which is the case here. A set of ancillary DFT tests confirmed this conclusion. For magnetic solutes (Cr, Fe and Mn), spin polarized calculations were performed assuming an initial spin moment of 5 μB. The Fe and Mn solutes retained magnetic moments in all sites explored following VASP minimization, while Cr solutes did not.

From the energy of the simulation cell containing the solute at (x_i, y_j) and dislocation, $E_{\text{disl+solute}}(x_i, y_j)$, the interaction energy is computed as

$$U\left(x_i, y_j\right) = E_{\text{disl+solute}}\left(x_i, y_j\right) - \left[E_{\text{disl only}} + E_{\text{ref}}\right] \tag{2.1}$$

where $E_{\text{disl only}}$ is the energy of the pure Al core and E_{ref} is the energy of a single solute in a bulk fcc Al crystal. Direct calculation of E_{ref} using the same simulation cell but containing undeformed fcc Al is not accurate, presumably due to differences in the surfaces effects/energies between the two geometries. For consistency with the core calculations, E_{ref} is estimated as the mean of the additional energy due to solutes in the 22 sites

$$E_{\text{ref}} = \frac{1}{22} \sum_i \sum_j \left(E_{\text{disl+solute}} \left(x_i, y_j \right) - E_{\text{disl only}} \right) \tag{2.2}$$

where the summations are over the 22 sites in the dislocation core considered in the DFT calculations. Due to asymmetry in the magnitude of the solute energies just above and below the stacking fault, this estimate of E_{ref} has some uncertainty. However, as will become clear later, the uncertainty in the predicted strength is second order in the uncertainty of E_{ref} and is small. For instance, in the case of Al-Mg alloys, an uncertainty of as much as 0.05 eV (a very large value) would result in only a 7% change in the predicted strength. Our estimate for E_{ref} also has the advantage of filtering out systematic errors in energy that are independent of solute position and further mitigates the boundary effects caused by not relaxing ions outside region I.

The effect of solute-solute interactions along the $\langle 1\bar{1}2 \rangle$ direction was explored by doubling the periodicity of the simulation cell along the line direction from 4.95 Å to 9.90 Å, thereby increasing the solute-solute spacing by the same amount. These simulations required a simulation cell containing $1,138$ ions. The solute interaction energies of supercells containing one and two solutes along the dislocation line at a few sites in the dislocation partial cores were calculated. The differences in interaction energies were minimal ($\approx 6\%$), consistent with EAM results on Al-Mg by Olmsted *et al.* [26] and

with the continuum prediction of zero interaction energy between two separate point dilatational sources.

It is not computationally feasible to calculate $U(x_i, y_j)$ on all sites using first-principles. However, away from the immediate core region, substitutional solutes are in a local fcc environment that is far less distorted than in the immediate core. Therefore, the continuum approximation of Eq. (1.2), $U(x_i, y_j) \approx -p(x_i, y_j)\Delta v_m$, should provide a good approximation of the interaction energies, particularly with increasing distance from the core region. However, the pressure field $p(x_i, y_j)$ must be that appropriate for the real dissociated core structure. One approach to computing $p(x_i, y_j)$ is to use the Peierls-Nabarro model, where the Burgers vector of the dislocation is distributed along the stacking fault using the differential displacements obtained from the dislocation geometry. We have used a related but simpler approach by spreading the Burgers vector into $n+1$ dislocations each of Burgers vector $b/(n+1)$ evenly spaced by $b/2$ over $n+1 = 11$ interstitial sites along the slip plane in the core region. The pressure field is then computed as

$$p(x_i, y_j) = -\frac{1+\nu}{3\pi\,(1-\nu)}\mu\frac{b}{n+1}\sum_{l=-n/2}^{n/2}\frac{y_j}{\left[x_i - l\left(\frac{b}{2}\right)\right]^2 + y_j^2}, \tag{2.3}$$

where ν is the Poisson's ratio of Al. This simple approximation was validated in EAM calculations of Al-Mg by Olmsted et al. [26].

Direct calculation of the misfit volume Δv_m through DFT volume relaxation calculations of perfect Al crystals containing a single solute atom shows inconsistent results between different supercell sizes. To obtain consistent results, we follow a more-complex method

TABLE 2.2: The misfit volume Δv_m for Mg, Cr, Si, Cu, Mn and Fe solutes in Al. Also shown are the predicted $T = 0$ yield stress τ_{y0} and energy barrier ΔE_b for each solute.

Solute	Δv_m (Å^3)	$\tau_{y0}/c^{2/3}$ (MPa)	$\Delta E_b/c^{1/3}$ (eV)
Mg	5.71	342	4.06
Cr	-11.68	705	6.65
Si	-2.65	137	2.58
Cu	-5.57	348	4.10
Mn	-13.31	711	7.53
Fe	-16.44	1072	8.20

to calculate Δv_m proposed by Vannarat *et al.* [47]. Using both 27-atom supercell and 64-atom supercells, internal geometry optimizations are performed with one, two and three solute atoms, and the change in pressure in these supercells was computed via DFT in VASP. The dependence of the pressure with concentration is very linear for all solutes considered, as shown in Figure 2.2, consistent with results in Ref. [47]. The misfit volume is then calculated using the slope of the pressure versus solute concentration and the DFT-computed bulk modulus B of Al,

$$\Delta v_m = \left(\frac{\partial \Delta v}{\partial c}\right) c_{1sol} = \left(\frac{1}{B}\frac{\partial p}{\partial c}\right) c_{1sol} \tag{2.4}$$

where c_{1sol} is the concentration of 1 solute in the supercell. The misfit volumes calculated using the two supercells differ by less than 15% across all the solutes considered, The misfit volume is taken as the average of the two derived values, and is shown in Table 2.2 for all solutes. The uncertainty in Δv_m causes uncertainties in the yield strength predictions of 10% or less.

Using the DFT results in the core and the continuum analytic model outside the core leads to the solute/dislocation energies $U_{ij} \equiv U(x_i, y_j)$ shown in Figure 2.3 for Mg,

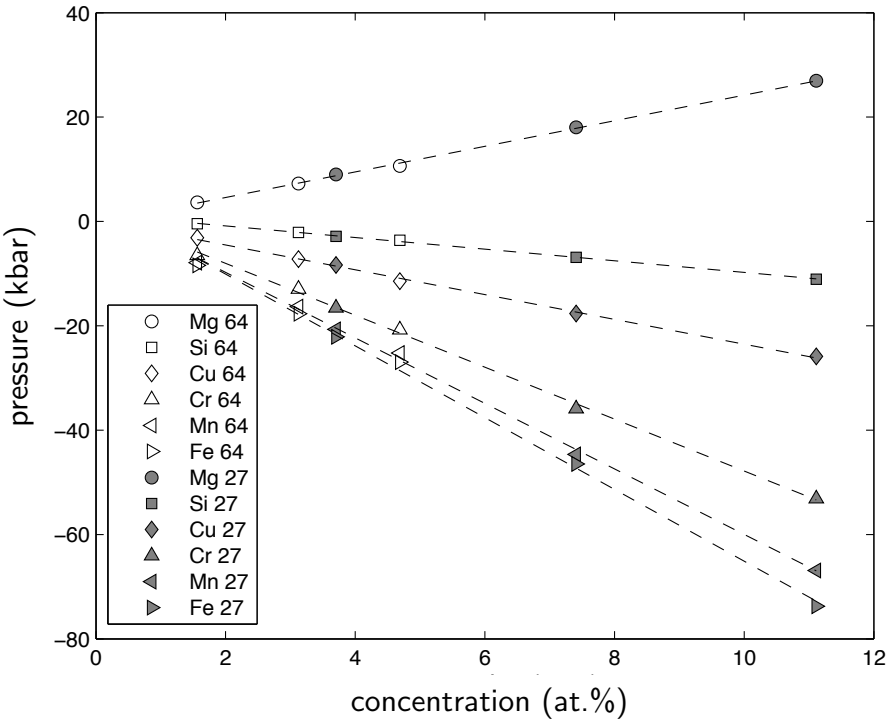

FIGURE 2.2: Pressure versus concentration in fixed-volume supercells containing solutes atoms, for Mg, Si, Cu, Cr, Mn and Fe solutes, for both 27- and 64-atom supercells. Dashed lines are linear fits using data from both supercells for each solute, and the slopes of these lines are used in Eq. (2.4) to compute the misfit volume.

Si, Cr, Cu, Mn and Fe solutes. Not surprisingly, solutes that are smaller ($\Delta v_m < 0$) than the host Al atom (Si, Cr, Cu, Mn and Fe) prefer to be on the compression side of the core while those that are larger (Mg) prefer to be on the tension side. The interaction energies are generally asymmetric between tension and compression in the layers immediately adjacent to the stacking fault. In most cases, there is a smooth transition between the DFT and the continuum regions, wherein the energies are highest in the immediate core region and decreases steadily with increasing distance from the core, The exceptions to this are Mn and Fe solutes, where the interaction energies in the second row are slightly higher than those in the core. In general, there are no sharp discontinuities in U_{ij} despite the different methodologies employed in calculating

the energies in the two regions, showing the consistency of the two approaches and the accuracy of $U(x_i, y_j) \approx p(x_i, y_j)\Delta v_m$ just outside the core region.

The first-principles computation of solute/dislocation interaction in the dislocation core is the first main result of this chapter. While a significant computational challenge with various subtleties, the interaction energies by themselves are insufficient to predict strengthening and so in the next section we turn our attention to a detailed model of solute strengthening that uses the interaction energies computed here as input.

2.3 Solute Strengthening Model

An initially straight dislocation of length L in a field of randomly-distributed solutes can lower its energy by bowing out into regions of the solid containing favorable fluctuations. The lateral length ζ of the favorable regions and their typical separation w along the slip direction must be determined by minimizing the total energy of the dislocation line. To make analytic progress, we simplify the possible dislocation configurations. In this simplified geometry, the dislocation is comprised of straight segments of length ζ lying in favorable local environments separated by roughening amplitude w along the slip direction, as depicted in Figure 2.4. Since it is generally not possible to abruptly transition from one favorable local environment to another, straight segments are connected to each other via additional segments of length ζ. For the case of $w \ll \zeta$, this geometry is close to a smooth piecewise sinusoidal dislocation configuration. In this geometry, the dislocation can be divided into $L/2\zeta$ unit cells, each with a segment of length ζ lying in an energetically favorable local environment.

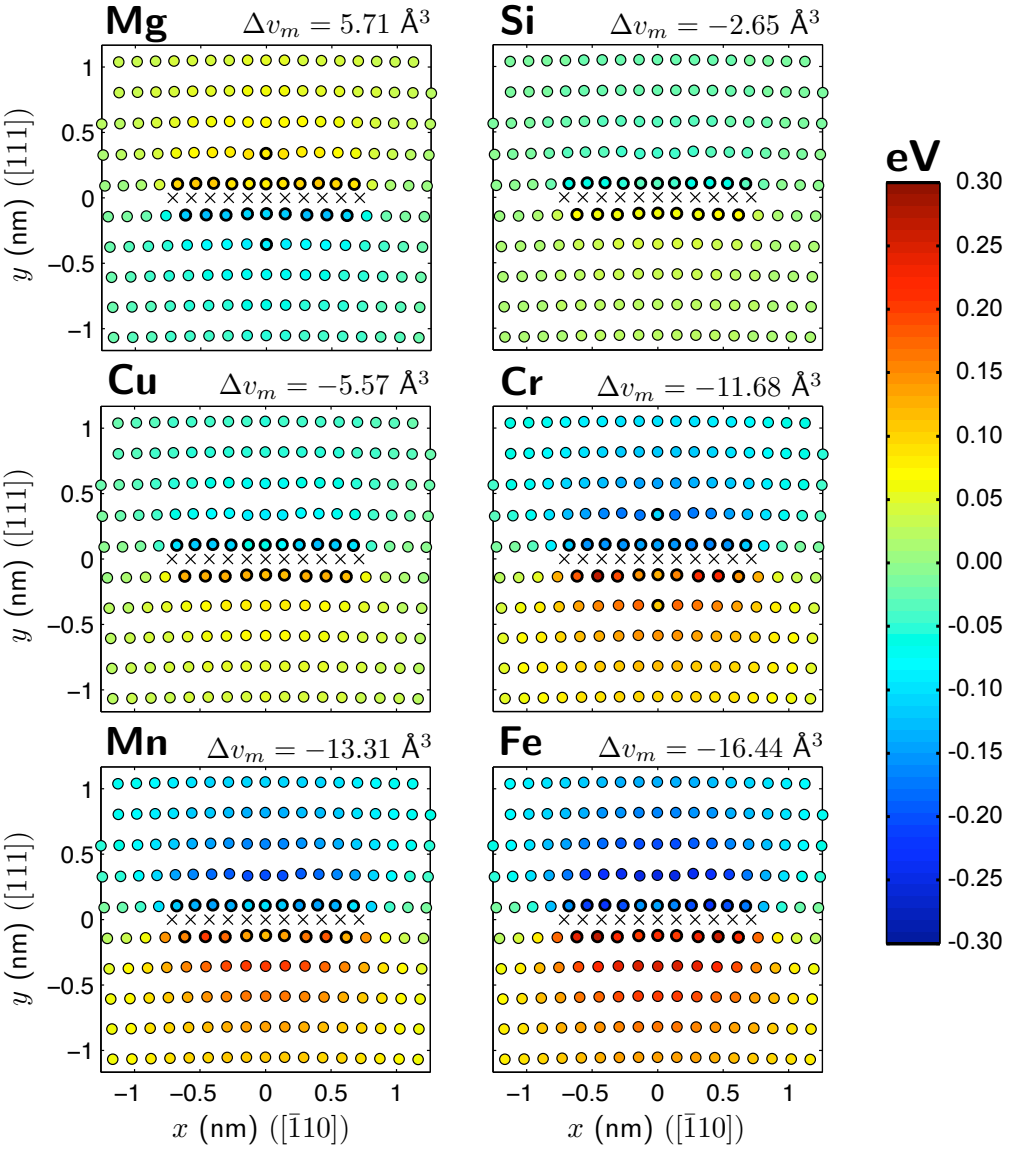

FIGURE 2.3: Solute/dislocation interaction energy U_{ij} versus solute position position (x_i, y_j) for Mg, Cr, Si, Cu, Mn and Fe solutes. Misfit volume Δv_m is shown for each solute. Negative energies indicate binding. Bold circles show positions at which first-principles interaction energies are calculated; "x" markers denote positions of the $b/11$ Burgers vector used to compute the analytic pressure field outside the immediate core sites (non-bold circles).

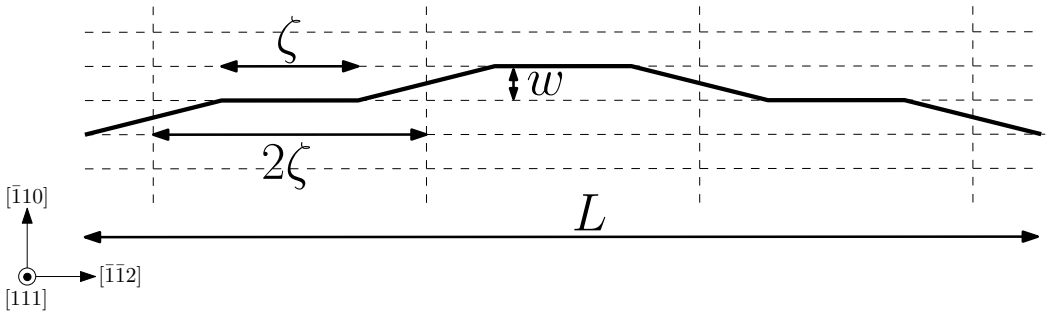

FIGURE 2.4: Schematic of a dislocation roughening into segments of length 2ζ with roughening amplitude w due to favorable solute fluctuations.

The change in total energy as the dislocation moves from the straight configuration to the bowed out configuration is the sum of the potential energy decrease due to solute/dislocation binding, ΔE_p, and the elastic energy increase due to the increase in line length, ΔE_{el},

$$\Delta E_{tot} = \Delta E_p + \Delta E_{el}. \tag{2.5}$$

For an isotropic line tension model with line tension Γ, the elastic energy is

$$\begin{aligned} \Delta E_{el} &= \Gamma \left[\left(\zeta^2 + w^2\right)^{\frac{1}{2}} - \zeta \right] \cdot \left(\frac{L}{2\zeta}\right) && (2.6) \\ &\approx \Gamma \left(\frac{w^2}{2\Gamma}\right)\left(\frac{L}{2\zeta}\right) && (2.7) \end{aligned}$$

since $w \ll \zeta$ is expected. Calculation of the binding energy due to solute fluctuations is more subtle, as noted in the Introduction, due to divergences that arise when simply summing the energies or fluctuation in energies. However, by recognizing that the total interaction energy as the dislocation segment moves between two positions is correlated over some distance, a finite, calculable solute binding energy and strength emerge

naturally without any need to truncate the range of interaction energies, as described below.

Consider a dislocation segment of length ζ in a random field of solutes. At each atomic position (x_i, y_j) projected in the plane normal to the dislocation line, there are n_{ij} solutes in the length ζ, where n_{ij} is a random number between zero and $N = \zeta/\sqrt{3}b$ (for a line direction of 110 in an fcc material). The energy of a segment at the origin is then

$$U_{tot}(\zeta) = \sum_{ij} n_{ij} U_{ij} \tag{2.8}$$

Moving the dislocation a distance w from the origin in the slip direction is equivalent to moving the solutes from (x_i, y_j) to $(x_i - w, y_j)$ while keeping the dislocation at the origin. The energy change, $\Delta U_{tot}(\zeta, w)$, of the dislocation segment of length ζ as it glides a distance w away from the origin can then be expressed as

$$\Delta U_{tot}(\zeta, w) = \sum_{ij} n_{ij} \Delta U_{ij}(w) \tag{2.9}$$

where $\Delta U_{ij}(w) = U(x_i - w, y_j) - U(x_i, y_j)$ and the summation in Eq. (2.8) extends to all in-plane sites. As noted earlier, the mean energy change $\langle \Delta U_{tot}(\zeta, w) \rangle$ vanishes for all values of w because $\langle n_{ij} \rangle = cN$ is constant, implying that the configurational force due to solute/dislocation interaction can only arise due to *spatial fluctuations* in solute concentration. Spatial fluctuations in solute concentration create a statistical distribution of total energies for a segment characterized by the standard deviation of Eq. (2.9),

$$\sigma_{\Delta U_{tot}}(\zeta, w) = \left[\left\langle \Delta U_{tot}(\zeta, w)^2 \right\rangle - \langle \Delta U_{tot}(\zeta, w) \rangle^2 \right]^{\frac{1}{2}}. \tag{2.10}$$

Some regions give rise to binding, $\sigma_{\Delta U_{tot}} < 0$, with characteristic energy $-\sigma_{\Delta U_{tot}}$, and others give rise to repulsion, $\sigma_{\Delta U_{tot}} > 0$ with characteristic energy $\sigma_{\Delta U_{tot}}$. Therefore, the characteristic potential energy decrease by allowing the dislocation segment to move into regions in the solid containing favorable solute fluctuations is

$$\Delta E_p = -\sigma_{\Delta U_{tot}} \cdot \frac{L}{2\zeta}. \tag{2.11}$$

To evaluate Eq. (2.10), we first express the first term on the right hand side of the equation as

$$\left\langle \Delta U_{tot}\left(\zeta, w\right)^2 \right\rangle = \left\langle n_{ij}^2 \right\rangle \sum_{ij} \Delta U_{ij}\left(w\right)^2 + \left\langle n_{ij} \right\rangle \left\langle n_{lm} \right\rangle \sum_{ij} \sum_{lm \neq ij} \Delta U_{ij}\left(w\right) \Delta U_{lm}\left(w\right) \tag{2.12}$$

since only n_{ij} is the random variable in the equation. The quantity $\left\langle n_{ij}^2 \right\rangle$ is given by the binomial theorem as

$$\left\langle n_{ij}^2 \right\rangle = \sum_{n=0}^{N} \frac{N!}{n!\left(N-n\right)!} p^n q^{1-p} n^2 \tag{2.13}$$

where p is the probability of finding a solute at position (x_i, y_j) which, for random solutes, is independent of position. Noting that $n^2 c^n = (p \cdot \partial/\partial p)^2 (p^n)$, $n_{ij} \leq N$ and that $p = c$, Eq. (2.13) reduces to

$$\left\langle n^2 \right\rangle = \left(cN\right)^2 + Nc(1-c) = \left\langle n \right\rangle^2 + c\left(1-c\right)N. \tag{2.14}$$

Substituting Eq. (2.14) into Eq. (2.12) yields

$$\begin{aligned}\left\langle \Delta U_{tot}\left(\zeta,w\right)^{2}\right\rangle &= \left[\left\langle n\right\rangle^{2}+c\left(1-c\right)N\right]\sum_{ij}\Delta U_{ij}\left(w\right)^{2} \\ &\quad +\left\langle n\right\rangle^{2}\sum_{ij}\sum_{lm\neq ij}\Delta U_{ij}\left(w\right)\Delta U_{lm}\left(w\right), \qquad (2.15)\\ &= c\left(1-c\right)N\sum_{ij}\Delta U_{ij}\left(w\right)^{2}+\left\langle \Delta U_{tot}\left(\zeta,w\right)\right\rangle^{2}. \qquad (2.16)\end{aligned}$$

Substituting Eq. (2.16) into Eq. (2.10) gives the expected fluctuation in the interaction energy when a segment of length ζ moves a distance w as

$$\sigma_{\Delta U_{tot}}\left(\zeta,w\right)=c\left(1-c\right)N\sum_{ij}\Delta U_{ij}\left(w\right)^{2}. \qquad (2.17)$$

The total average binding energy of a dislocation due to solute/dislocation interaction is then obtained by substituting Eq. (2.17) into (2.11). For low concentrations $c\ll 1$,

$$\Delta E_{p}\left(\zeta,w\right)=-\left[\left(\frac{c\zeta}{\sqrt{3}b}\right)^{\frac{1}{2}}\Delta\tilde{E}_{p}\left(w\right)\right]\cdot\left(\frac{L}{2\zeta}\right) \qquad (2.18)$$

where

$$\Delta\tilde{E}_{p}\left(w\right)=\left[\sum_{ij}\left(U\left(x_{i}-w,y_{j}\right)-U\left(x_{i},y_{j}\right)\right)^{2}\right]^{\frac{1}{2}}. \qquad (2.19)$$

Equation (2.19) can be rearranged into the form

$$\Delta\tilde{E}_{p}\left(w\right)=\left[2\sum_{ij}\left(1-\chi\left(w,y_{j}\right)\right)U\left(x_{i},y_{j}\right)^{2}\right]^{\frac{1}{2}} \qquad (2.20)$$

where

$$\chi\left(w,y_{j}\right)=\frac{\sum_{k}U\left(x_{k}-w,y_{j}\right)U\left(x_{k},y_{j}\right)}{\sum_{k}U\left(x_{k},y_{j}\right)^{2}}. \qquad (2.21)$$

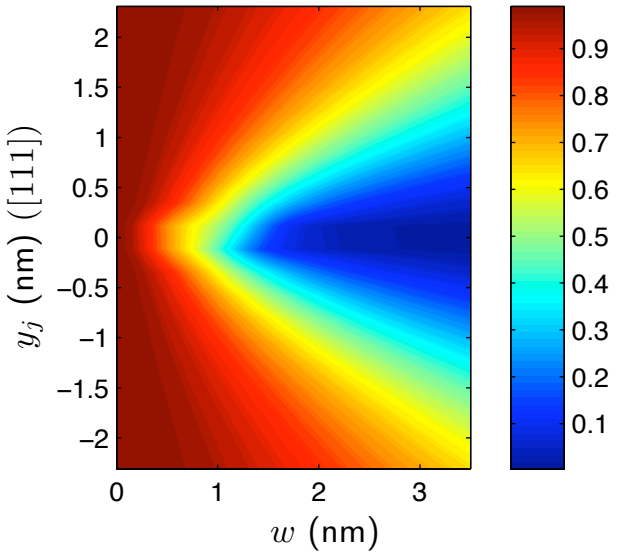

FIGURE 2.5: Energy correlation function $\chi(w, y_j)$ for a solute initially at $(0, y_j)$ as the dislocation moves a distance w, as computed for an Al-Mg alloy.

is the correlation function between the interaction energies of a solute at y_j before (x_i) and after $(x_i - w)$ the dislocation glides w away from its original position. For any finite w, the correlation $\chi(w, y_j)$ increases as $|y_j|$ increases, i.e. the interaction energies of a solute far from the dislocation are highly correlated, $\chi(w, y_j) \to 1$, as shown in Figure 2.5. Such solutes therefore do not contribute significantly to the change in total energy. The quantity $\Delta\tilde{E}_p(w)$ is thus finite and there is no need to introduce any artificial truncation in the range of the solute/dislocation interactions.

Substituting Eq. (2.6) and Eq. (2.18) into Eq. (2.5) gives the total energy change as a function of ζ and w, for a dislocation taking on the configuration depicted in Figure 2.4, as

$$\Delta E_{tot}(\zeta, w) = \left[\left(\Gamma\frac{w^2}{2\zeta}\right) - \left(\frac{c\zeta}{\sqrt{3}b}\right)^{\frac{1}{2}} \Delta\tilde{E}_p(w)\right] \cdot \left(\frac{L}{2\zeta}\right). \tag{2.22}$$

To obtain the equilibrium configuration of the dislocation, we minimize Eq. (2.22) with

respect to ζ and w. Analytic minimization with respect to ζ is straightforward, yielding the characteristic segment ζ_c as a function of the roughening amplitude w given by

$$\zeta_c(w) = \left(4\sqrt{3} \frac{\Gamma^2 w^4 b}{c \Delta \tilde{E}_p^2(w)} \right)^{\frac{1}{3}}. \tag{2.23}$$

Substituting this expression into Eq. (2.22), the total energy is now solely a function of the roughening amplitude w,

$$\Delta E_{tot}\left(w, \zeta_c(w)\right) = -\frac{3^{2/3}}{8\ 2^{1/3}} \left(\frac{c^2 \Delta \tilde{E}_p^2(w)}{b^2 w^2 \Gamma} \right)^{\frac{1}{3}} L. \tag{2.24}$$

Minimizing $\Delta E_{tot}\left(w, \zeta_c(w)\right)$ with respect to w yields the equilibrium energy and a characteristic amplitude w_c. This minimization cannot be done analytically and so must be done numerically. Scaling out the concentration, the total energy per unit length $\Delta E_{tot}/Lc^{2/3}$ versus w is shown in Figure 2.6. Figure 2.6 also shows the convergence of $\Delta E_{tot}/Lc^{2/3}$ as a function of the upper limit of the summation over y_j, which demonstrates that (i) the characteristic value w_c is established quite well by the core sites only (y_1 and y_{-1}), (ii) the sum converges quickly with increasing number of layers of sites (increasing j), and (iii) the magnitude of the contributions from sites within the core (y_1,y_{-1}) and outside the core ($y_j, |j| > 1$) are approximately equal, with significant contributions for $|j| = 2, 3$. Point (i) above demonstrates that the core structure is crucial for obtaining w_c, justifying the computational expense of DFT in this region, but point (iii) shows that the region outside the core is also crucial for obtaining an accurate total energy. Calculations for other solutes yield the same general conclusions but with w_c varying slightly (1.57 nm for Mg, Si and Cu; 1.71 nm for Cr and Fe; and 1.86 nm for

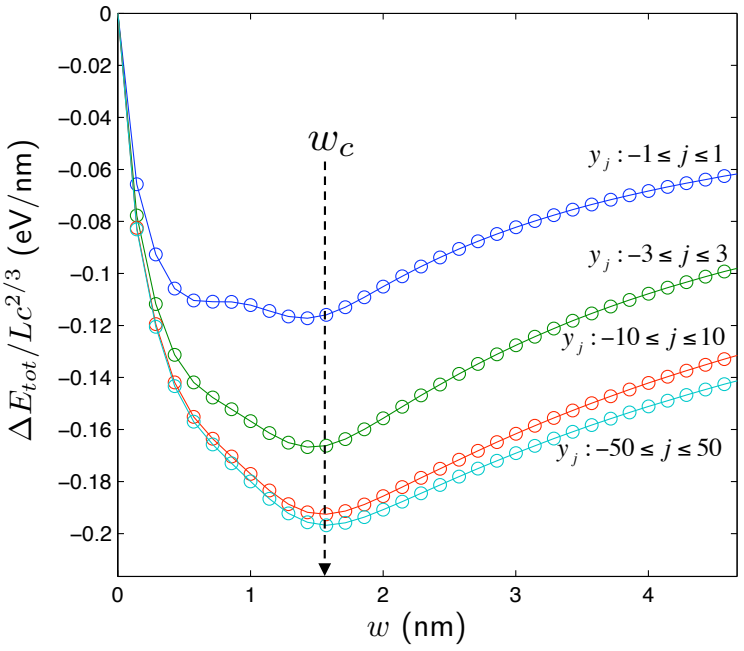

FIGURE 2.6: Normalized total energy per unit length $\Delta E_{tot}/Lc^{2/3}$ versus roughening amplitude w for an Al-Mg alloy, for various partial sums over solute sites y_j demonstrating the dominance of the core region y_{-1}, y_1 and convergence of the total energy with increasing range of $|y_j|$.

Mn) in spite of a large range of misfit volumes among these solutes. The values of w_c are approximately equal to 1.5 times the core width, so that when the dislocation moves by w_c, it encounters a new set of solutes in the core that create a binding energy that is statistically uncorrelated with the energy at the prior position.

After minimization, we have a final total energy per unit length of $\Delta E_{tot}\left(w_c, \zeta_c(w_c)\right)/L$. The relevant characteristic energy is the energy associated with each pinned segment of length ζ_c and the surrounding length of ζ_c (see Figure 2.4), which is thus, from Eqs. (2.23) and (2.24),

$$\Delta E_c = \Delta E_{tot}\left(w_c, \zeta_c(w_c)\right)\frac{2\zeta_c}{L} = -\frac{3^{5/6}}{2^{5/3}}\left(\frac{cw_c^2\Gamma\Delta\tilde{E}_p^2(w_c)}{b}\right)^{\frac{1}{3}}. \tag{2.25}$$

Although ΔE_c is the characteristic energy, it is not the energy barrier for determining thermally activated motion of the dislocation. ΔE_c is the typical energy change on moving from one *arbitrary* point to another point w_c away. The dislocation is pinned in a local minimum and must escape over the adjacent local maximum, in an energy landscape with a characteristic energy ΔE_c. Thus, the energy barrier ΔE_b is typically larger than ΔE_c, and is determined as follows. First we note that the elastic energy contribution to ΔE_b is the same as to ΔE_c. We thus concentrate on the potential energy contribution ΔE_p to ΔE_b. The potential energy landscape, i.e. the energy versus dislocation position (x, y=0) along the glide plane of the dislocation segment of length ζ_c, can locally be approximated as a sinusoid with some amplitude $\Delta E_b'$, i.e.

$$E\left(x\right) = \frac{\Delta E_b'}{2}\left[1 - \cos\left(\frac{\pi x}{w_c}\right)\right]. \tag{2.26}$$

where $\Delta E_b'$ is the potential energy barrier. From our discussion above, ΔE_p is the standard deviation of the change in energy of the dislocation segment as it moves w_c away,

$$\Delta E_p = \left[\frac{1}{2w_c}\int_0^{2w_c}\left(E\left(x - w_c\right) - E\left(x\right)\right)^2 dx\right]^{\frac{1}{2}} = \frac{1}{\sqrt{2}}\Delta E_b'. \tag{2.27}$$

Thus, the typical potential energy barrier $\Delta E_b'$ is $\sqrt{2}$ times larger than ΔE_p. The total energy barrier includes the elastic energy contribution, and so is given by

$$\Delta E_b = \Delta E_b' - \Delta E_{el} = \left(\frac{4\sqrt{2}-1}{3}\cdot\frac{3^{5/6}}{2^{5/3}}\right)\left(\frac{cw_c^2\Gamma\Delta\tilde{E}_p^2(w_c)}{b}\right)^{\frac{1}{3}}. \tag{2.28}$$

The sign convention in Eq. (2.28) is opposite of that in Eq. (2.25) because the latter refers to the energy change due to the bowing out process while the former refers to the

magnitude of the energy barrier.

We validate the above analysis showing that $\Delta E_b' = \sqrt{2}\Delta E_p$ using a stochastic simulation of a straight dislocation moving through a random field of solutes. Remaining straight, only the potential energy ΔE_p is computed. A segment of length $\zeta = 18.06$ nm is placed in a simulation box of size 1425nm x 5.12nm x 18.06nm containing a 5 at.% Mg solutes randomly distributed. This simulation box is large enough such that the relative potential energy differences with position within w_c are converged. The total potential energy of the straight dislocation is calculated as a function of dislocation position along the glide plane in the simulation box, as shown in Figure 2.7(a). The expected standard deviation $\pm\Delta E_p$ as calculated analytically is shown in Figure 2.7(a) and agrees well with the simulated result; this is not surprising. Locally, the energies in Figure 2.7(a) are sinusoidal and the typical energy barrier, from a local minimum to a local maximum, is larger than ΔE_p. The energy barriers are best probed by examining the resisting stress exerted by the solutes on the dislocation, which is equal to the spatial derivative of ΔE_p with respect to x, $\tau_{resist} = -(1/b\zeta)(\partial \Delta E_p/\partial x)$, and is shown in Figure 2.7(b). The maximum and minimum values of τ_{resist} are related to the underlying energy barrier $\Delta E_b'$ as

$$\tau_{resist}^{max/min} = \frac{\pi}{2}\frac{\Delta E_b'}{b\zeta w_c}. \tag{2.29}$$

The predicted values of $\tau_{resist}^{max/min}$ using $\Delta E_b' = \sqrt{2}\Delta E_p$ are shown in Figure 2.7(b) and agree well with the simulated values, thus validating the analytic result.

We have determined that dislocation segments of length ζ_c (Eq. (2.23)) are pinned in typical energy minima with barriers of height ΔE_b (Eq. (2.28)) over a length w_c (e.g. Figure 2.6). We can now use standard analyses of thermally-activated dislocation motion

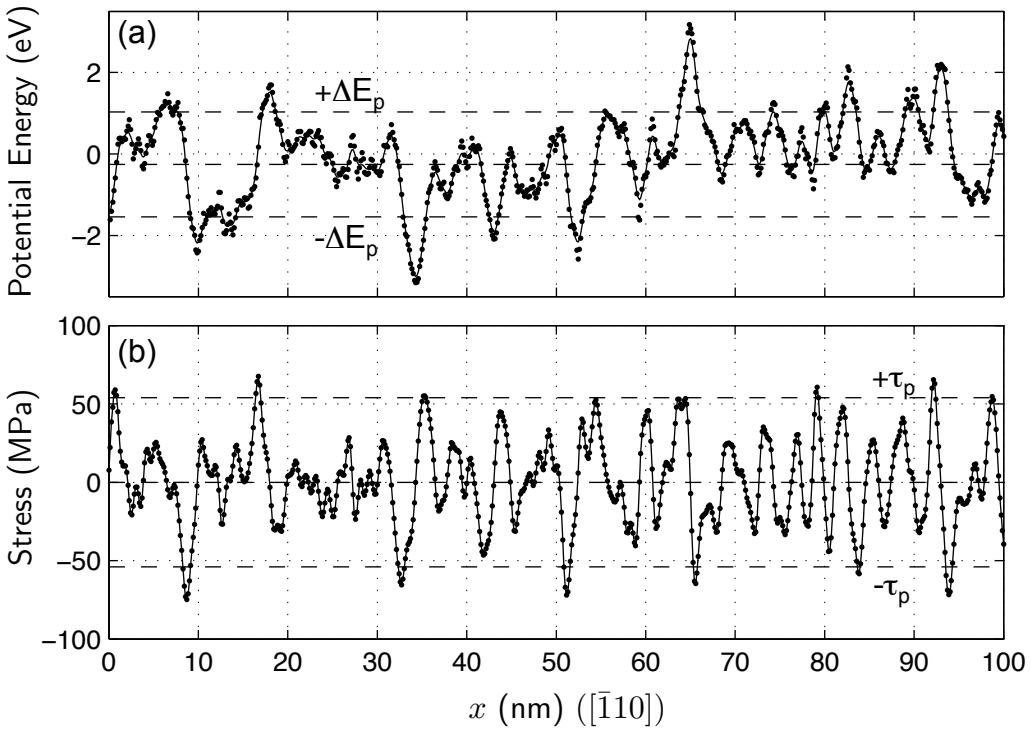

FIGURE 2.7: (a) Energy versus position of a straight dislocation segment of length $\zeta = 18.06$ nm moving through a random 5 at.% Mg solute field; (b) Stress required to move the dislocation across the energy landscape.

to determine the finite-T and rate-dependent yield stress, as follows. When the material is subjected to an applied resolved shear stress τ, the energy landscape $E(\tau, x)$ must be modified to include the work done by the applied stress, and so becomes

$$E(\tau, x) = \frac{\Delta E_b}{2}\left[1 - \cos\left(\frac{\pi x}{w_c}\right)\right] - \tau\zeta_c b x. \tag{2.30}$$

. The stress-dependent barrier height $\Delta E(\tau)$ can be approximated (within 6%) by [21]

$$\Delta E(\tau) \approx \Delta E_b\left[1 - \left(\frac{\tau}{\tau_{y0}}\right)\right]^{\frac{3}{2}}. \tag{2.31}$$

Here, τ_{y0} is the zero-temperature yield strength, i.e. the stress at which the energy landscape exhibits no barrier for dislocation motion,

$$\tau_{y0} = \frac{\pi}{2}\frac{\Delta E_b}{b\zeta_c(w_c)w_c} = 1.01\left(\frac{c^2\Delta\tilde{E}_p^4(w_c)}{\Gamma b^5 w_c^5}\right)^{\frac{1}{3}} \tag{2.32}$$

with $1.01 = \pi\left(4\sqrt{2}-1\right)/3^{1/3}2^{10/3}$ a constant containing all the numerical factors. At finite temperature, the dislocation can be thermally activated over the barrier at stresses below τ_{y0}. Using the same arguments as that stated in Section 1.4, the finite temperature stress required for dislocation flow is given by

$$\tau_y(T) = \tau_{y0}\left[1-\left(\frac{kT}{\Delta E_b}\ln\frac{\dot{\epsilon_\circ}}{\dot{\epsilon}}\right)^{\frac{2}{3}}\right]. \tag{2.33}$$

Equation (2.33) applies at low T but not at cryogenic T where dynamic effects can enter [21]. At high T, Labusch has shown that the characteristic length ζ_c effectively increases as the dislocation can explore other configurations, but with the behavior still controlled by the energy barrier ΔE_b. Over a wide range of temperature, $0.2 < kT\ln\left(\dot{\epsilon_\circ}/\dot{\epsilon}\right)/\Delta E_b < 0.6$, this result of Labusch can be matched to Eq. (2.33) as

$$\tau_y\left(T\right) = \tau_{y0}\exp\left(-\frac{1}{0.51}\frac{kT}{\Delta E_b}\ln\frac{\dot{\epsilon_\circ}}{\dot{\epsilon}}\right) \tag{2.34}$$

where the parameter 0.51 provides a good fit ($< 7\%$) to both Eq. (2.33) and its derivative with respect to T. While nearly identical over a range of temperature, Eq. (2.34) does not reach zero at any finite temperature, and is thus more accurate at elevated temperatures. Eqs. (2.28), (2.32), (2.33)–(2.34) are the second main results of this chapter.

Associated with thermally-activated flow is the activation volume $V = -\partial\Delta E/\partial\tau$, which

is the area swept out by the dislocation during the activation process multiplied by the Burgers vector. The activation volume can be measured experimentally using strain rate jump tests and other methods and is a sensitive measure of the response of the material that can provide insight into underlying mechanisms [1]. Taking the derivative of Eq. (2.31) with respect to τ yields

$$V(T) = -\frac{\partial E_0}{\partial \tau} = \frac{3}{2}\frac{\Delta E_b}{\tau_{y0}}\left(\frac{kT}{\Delta E_b}\ln\frac{\dot{\epsilon}_0}{\dot{\epsilon}}\right)^{\frac{1}{3}}. \tag{2.35}$$

Experimentally, a direct relationship between V and the finite temperature yield stress τ_y has been observed. This led Basinski to postulate the so-called "stress equivalency principle": if two different alloys have the same τ_y at the same temperature T and strain rate $\dot{\epsilon}$, then they will also have the same V, regardless of the concentrations and types of solutes in the two different alloys [48]. "Stress equivalency" is satisfied by the present model under some weak constraints. Specifically, if the roughening amplitude w_c varies only mildly with the type of solute in the alloy, then the parameter $c\Delta\tilde{E}_p^2$ controls the values of both τ_{y0} and ΔE_b, which in turn govern both V and τ_y. Equation (2.33) can then be rewritten as a function of V,

$$\tau_y = 2.23\left(\frac{bkTw_c^3\Gamma\eta}{V^3}\right)^{\frac{1}{2}}\left[1 - 0.67\left(\frac{kT\eta}{\left(\frac{b^3kTw_c^9\Gamma^3\eta}{V}\right)^{\frac{3}{4}}}\right)^{\frac{2}{3}}\right] \tag{2.36}$$

where $\eta = \ln(\dot{\epsilon}_0/\dot{\epsilon})$. The activation volume V and the finite temperature flow stress τ_y are thus related by an equation of the form $\tau_y = AV^{-2/3}(1 - BV^{-1/2})$, where A and B are constants. If $B \ll 1$, then V and τ_y are related by a simple power law, $V \sim \tau_y^{2/3}$, which was previously derived for the Labusch model by Nabarro [49]. For different

solutes with the same w_c, Basinski's stress equivalency principle is thus strictly obeyed. Slight variations in w_c will be manifested as slight rigid shifts preserving the functional form; for all materials studied in this chapter, these shifts are small. The activation volume is also predicted to scale as $c^{-\frac{4}{9}}$, which is close to the $\sim c^{-\frac{1}{2}}$ trend reported in the literature [1].

The present model is easily generalized to consider more than one solute. For an arbitrary number of random non-interacting solutes, Eq. (2.8) is replaced by

$$\Delta U_{tot}(\zeta, w) = \sum_{ij} \left(n_{ij}^{(1)} \Delta U_{ij}^{(1)}(w) + n_{ij}^{(2)} \Delta U_{ij}^{(2)}(w) + n_{ij}^{(3)} \Delta U_{ij}^{(3)}(w) \dots \right) \tag{2.37}$$

where the superscripts indicate the type of solutes. For the multisolute case, the analysis above then applies with $c\Delta\tilde{E}_p^2$ replaced by $\sum_i c_i \Delta\tilde{E}_p^{(i)2}$. For solutes with the same w_c, the zero temperature strength and characteristic energy barrier are

$$\tau_{y0} = \left[\sum_i \left(\tau_{y0}^{(i)} \right)^{\frac{3}{2}} \right]^{\frac{2}{3}}, \tag{2.38}$$

$$\Delta E_b = \left[\sum_i \left(\Delta E_b^{(i)} \right)^3 \right]^{\frac{1}{3}}, \tag{2.39}$$

the former consistent with Labusch's analysis. Numerical minimization must be used for solutes with different w_c to determine the effective w_c but the difference between direct minimization and Eq. (2.39) is small for all the solutes considered in this chapter. For instance, the differences in τ_{y0} and ΔE_b between numerical minimization and Eq. (2.39) for a 1% Mg ($w_c = 1.57nm$)/1% Mn ($w_c = 1.86nm$) alloy are 5% and 4%, respectively.

The theory presented in this section utilizes the fundamental solute/dislocation energies

as input into a detailed model that culminates in the prediction of the characteristic energy barrier and length scales for dislocation motion through the material. Use of first-principles data overcomes the problem of lack of knowledge of solute interactions in the core of the dislocation. Careful analysis of the correlations in solute fluctuations overcomes the apparent problem of diverging energies that inhibited earlier approaches from being parameter-free. From these fundamental properties, the finite-T, rate-dependent yield stress follows naturally via thermal-activation theory, with no adjustable parameters at any stage. The model is related conceptually to the classic Labusch model, predicting similar scalings with concentration, stress-equivalency, and generalized to multiple solute types, but has succeeded in eliminating ad-hoc features and fitting of parameters used in prior implementations of the Labusch concepts. We next turn to predictions of the model when applied to Al-X alloys to demonstrate the quantitative predictability of the model.

2.4 Results and Discussion

Using the interaction energies calculated in Section 2.2 and the strengthening model presented in Section 2.3, the zero temperature stress scaled by concentration, $\tau_{y0}/c^{2/3}$, and the energy barrier scaled by concentration, $\Delta E_b/c^{1/3}$, are presented in Table 2.2 for Mg, Si, Cu, Cr, Mn and Fe solutes in Al. The line tension used, $\Gamma = 0.47$ eV/Å, is based on new robust molecular statics calculations on EAM Al [50]. The quoted values in Table 2.2 have an estimated uncertainty of 5–10% due to uncertainties in the reference interaction energy, E_{ref}, and the computed misfit volumes, Δv_m. Using Eqs. (2.38)–(2.39) and Eq. (2.33), the finite temperature flow stress of an alloy containing

any number of these solutes can be predicted, with no parameters. Modifications to the detailed analysis in Section 2.3 could lead only to a shift by an overall constant factor independent of solute type or concentration.

The experimental flow stress values of 12 distinct and well-characterized Al-X alloys have been measured at $78K$ and $\dot{\epsilon} = 3 \times 10^{-5}\ s^{-1}$ by Diak *et al.* [1–3]. Values for $\dot{\epsilon_\circ}$ typically range from 10^4–10^6 s^{-1}; appearing in a logarithm, the precise value is not crucial and we use 10^4 s^{-1}. The flow stresses are measured using a 0.02% strain offset, corresponding to the onset of plastic flow associated with dislocation motion in tension tests on polycrystalline materials. The predicted shear flow stresses must therefore be multiplied by the Taylor factor $M = 3$ in order to compare with experiments.

Table 2.3 shows the predicted and experimental flow stresses for all nominally binary Al-X alloys Predictions for the Al-Mg alloys are in very good agreement with experimental values, being only $\sim 15\%$ lower. Predictions for the Al-Mn alloys are similarly close to the experimental values. In contrast, the Al-Fe alloys containing parts per million (ppm) of Fe solutes are drastically underestimated, with predictions of virtually zero strength and experiments showing strengths on the order of 10's of MPa. It is clear that the strengthening due to dilute Fe solutes cannot be explained by the interaction energies calculated in Section 2.2 and the model of Section 2.3. The predicted strengths for the Al-Cr and Al-Cu alloys are rather smaller than experiments although the general trends are captured. For instance, the Al-Cu and Al-Cr alloys with similar solute concentrations have strengths differing by approximately a factor of two in both predictions and experiments. The difference between theory and experiment for these two alloys lies in the presence of ppm Fe in these nominally binary alloys.

TABLE 2.3: Predicted and experimental [1, 2] tensile yield stresses at $T = 78K$ for various Al-X alloys. Solute concentrations are from Diak et al. [1, 2].

Solute	c (%)	Tensile Yield Stress σ_y (MPa)	
		Predicted (78K)	Experiment (78K)
Mg	0.444	18.2	20.6
Mg	0.810	28.9	34.2
Mn	0.123	17.1	20.8
Mn	0.246	28.8	28.9
Mn	0.494	48.1	44.0
Fe	7.7×10^{-4}	0.1	11.0
Fe	16.9×10^{-4}	0.5	16.7
Fe	43.5×10^{-4}	1.6	33.4
Cr-(Fe)	0.073 (10×10^{-4})	11.0	23.7
Cr-(Fe)	0.302 (12×10^{-4})	32.5	50.2
Cu-(Fe)	0.090 (12×10^{-4})	5.3	12.3
Cu-(Fe)	1.650 (50×10^{-4})	51.1	86.6

It is beyond the scope of this chapter to address the Al-Fe system in more detail, which will be done in a subsequent publication. We can, however, account for the role of Fe in the nominally binary Al-Cr-(Fe) and Al-Cu-(Fe) alloys using the experimental results for Al-Fe, as follows. The experimental yield stresses for Al-Fe do scale reasonably well with $c^{2/3}$ suggesting that Labusch scaling applies to the Fe solutes despite the anomalous magnitude. We thus use the experimental yield stresses at T=78K to back-calculate an effective value for $c\Delta\tilde{E}_p^2$ for Al-Fe, from which we then obtain experimentally-derived values of $\tau_y/c^{2/3} = 13,238MPa$ and $\Delta E_b/c^{1/3} = 28.8eV$. Predictions for the Al-Cr-(Fe) and Al-Cu-(Fe) alloys using the theory plus the experimentally-derived parameters for Fe are shown in Table 2.4, and good agreement with experiments is now obtained for all cases.

Figure 2.8 shows the experimental yield stress versus the predicted value for all of the alloys except Al-Fe, graphically demonstrating consistent agreement across the entire range of alloys at T=78K. Diak *et al.* have also recently measured the yield stresses of

TABLE 2.4: Predicted and experimental [1, 2] tensile yield stresses at $T = 78K$ for Al-Cr and Al-Cu alloys containing additional Fe solutes, using experimentally-derived parameters for Fe.

Solute	c (%)	Tensile Yield Stress σ_y (MPa)	
		Predicted (78K)	Experiment (78K)
Cr-(Fe)	0.073 (10×10^{-4})	19.4	23.7
Cr-(Fe)	0.302 (12×10^{-4})	39.8	50.2
Cu-(Fe)	0.090 (12×10^{-4})	16.7	12.3
Cu-(Fe)	1.650 (50×10^{-4})	75.8	86.6

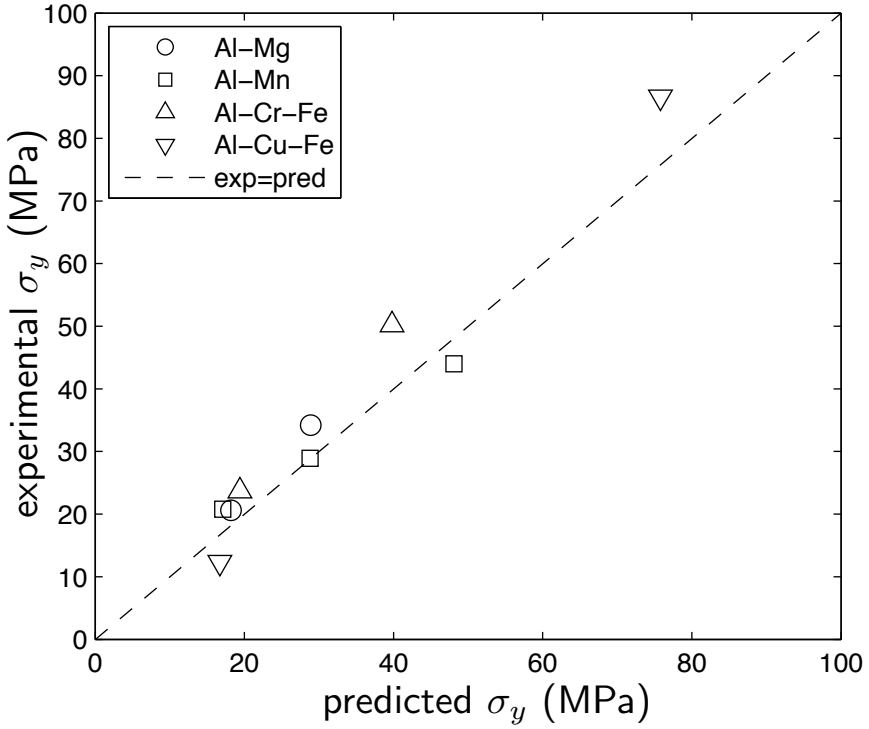

FIGURE 2.8: Experimental [1–3] versus predicted flow stress σ_y for 9 distinct alloys, showing overall good agreement. The dashed line has a slope of unity and indicates perfect agreement.

the Al-Mn alloys at several elevated temperatures [3]. Using the parameters in Table 2.2 and the theory of Eq. (2.34), predictions of the model are compared against experiment for the Al-Mn system at three temperatures in Figure 2.9. The agreement is again very good over the entire range although there is a small systematic deviation.

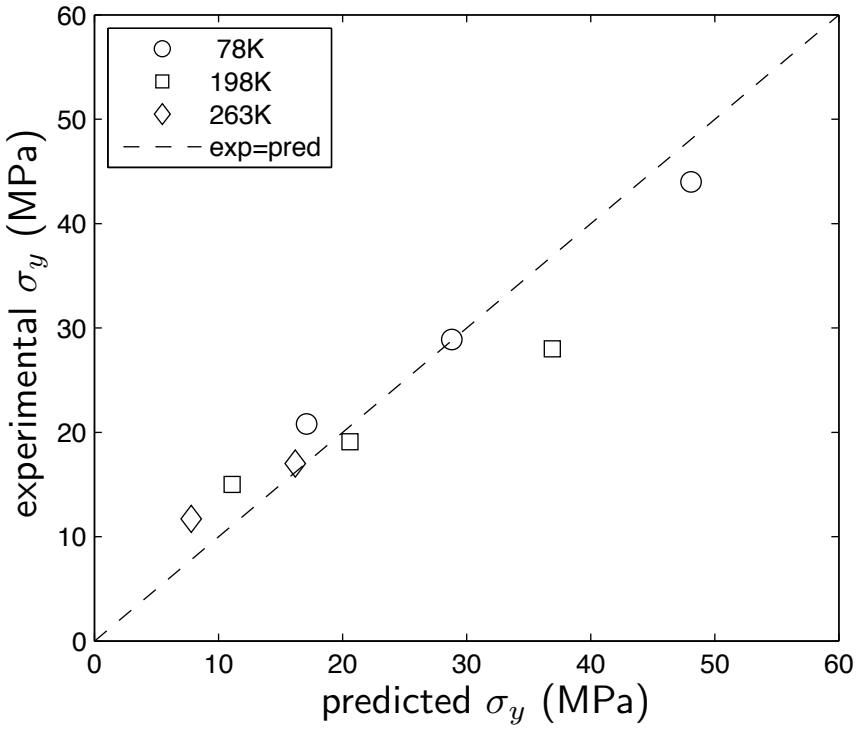

FIGURE 2.9: Experimental [3] versus predicted flow stress σ_y for 3 Al-Mn alloys at 78K, 198K and 263K, showing overall good agreement. The dashed line has a slope of unity and indicates perfect agreement.

Diak and colleagues measured the activation volumes of some of the alloys listed in Table 2.3 [1, 2]. Figure 2.10 shows the activation volume MV/b^3 versus the T=78K shear yield stress $\tau_y = \sigma_y/M$ in log-log form to elucidate any power-law scaling and stress equivalency. The predicted V are of the same magnitude as the experimentally measured values but typically over-estimate the experiments by roughly a factor of two. We consider this parameter-free prediction to be in good agreement with experiments because the activation volume reflects the product $b\zeta_c w_c$ that involves the two key length scales emerging from the theory. The predicted values fall nearly along a single curve, reflecting the stress-equivalency principle with the small variations attributable to differences in w_c among alloys. Both experiments and predictions are approximately linear,

indicating power-law scaling, but the slopes indicate two different power-laws, $V \sim \tau_y^{-0.6}$ is predicted while the experimental trend is $V \sim \tau_y^{-1.0}$. One possible source of the discrepancy between experimental and predicted activation volumes is associated with the value of the line tension Γ. The finite temperature stress $\tau_y(T)$ is only weakly dependent on Γ because the zero temperature yield stress scales as $\Gamma^{-1/3}$ and the energy barrier scales as $\Gamma^{1/3}$, and these opposite dependencies on Γ partially cancel. However, the activation volume depends on the ratio of these quantities, and scales as $\Gamma^{5/9}$. A line tension Γ smaller than the EAM-Al-derived value of $\Gamma = 0.47eV$ would decrease the predicted activation volumes by a constant factor, with a rather smaller decrease in predicted yield stress. Additionally, non-solute related strengthening mechanisms, such as a Peierls barrier, can influence the slope of the experimentally-measured V without having too much effect on the yield stress itself. Overall, reasonable agreement in the values for V supports the model presented here.

2.5 Conclusion

We have shown that first-principles calculations of the interaction energy coupled with a parameter-free solute strengthening model leads to predicted flow stresses that agree with experiments over a wide range of Al alloys. The model both resolves fundamental difficulties encountered in existing literature models and avoids introducing any adjustable parameters. Previous predictions using first-principles input were limited to zero temperature flow stresses and provided little insight into the temperature and strain-rate dependence of the strengthening.

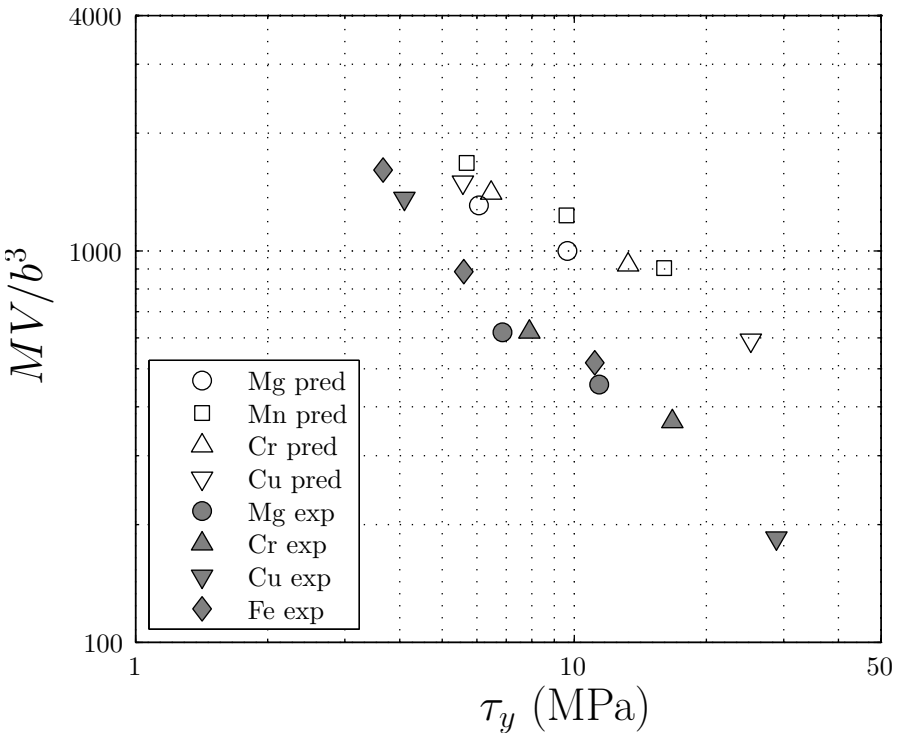

FIGURE 2.10: Normalized activation volume MV/b^3 versus 78K shear yield stress τ_y for both experimental [1] and predicted results, in log-log form, demonstrating stress equivalency.

While the results obtained from the model are promising, the model only applies to moderate solute concentrations where Mott/Labusch statistics apply. For extremely dilute concentrations, Friedel statistics govern the strengthening behavior or solutes, and a point pinning model such as the one presented in Ref. [4] may be more applicable. It is therefore important to better understand the transition between these two regimes. Previous literature has explored this transition but a quantitative determination of the transition is yet to be achieved. Possibly related to this issue is the anomalous behavior of dilute Fe in Al. The high strengthening of Fe, relative to predictions here and all other solute additions, has implications for alloy design and processing, and so must be better understood.

In the absence of first-principles input, for other solutes or other host materials than those studied here, the analytic model here can be treated as a two-parameter model in terms of the zero temperature flow stress τ_{y0} (Eq. (2.32)) and the energy barrier ΔE_b (Eq. (2.28)). This is just a consequence of thermal activation theory. More subtle is the fact that τ_{y0} and ΔE_b depend on the fundamental parameters $c\Delta\tilde{E}_p^2$ and w_c. If w_c is taken as 1.5 times the core width for a given host, then the model here reduces to a one-parameter theory. Experimental data can then be compared to predictions in which $c\Delta\tilde{E}_p^2$ is used to fit temperature- and/or concentration-dependent data.

An alternative simple approach also emerges by interpreting our results from a pure continuum elasticity perspective. While formally inadequate in the core, continuum elasticity suggests that $\Delta\tilde{E}_p \sim \Delta v_m$, and thus that $\tau_{y0} \sim \Delta v_m^{4/3}$ and $\Delta E_b \sim \Delta v_m^{2/3}$. Our full first-principles data, culminating in the results of Table 2.2, follows this scaling fairly closely:

$$\tau_{y0}/c^{2/3} \approx \left(31.1 \pm 6.3 \text{ MPa/Å}^4\right) \Delta v_m^{4/3}, \tag{2.40}$$

$$\Delta E_b/c^{1/3} \approx \left(1.31 \pm 0.03 \text{ eV/Å}^2\right) \Delta v_m^{2/3}. \tag{2.41}$$

Thus, it may be possible to use inexpensive first-principles methods to compute the surrogate material parameter Δv_m. For new host matrix materials, the coefficients above would be unknown, but fitting to limited experimental data on one solute might reveal the coefficient, which would then permit application to other solutes or combinations of solutes. However, the variations in Eq. (2.40) suggest that such an approach has limited accuracy, with predictions of the zero-temperature strength deviating by up to $\pm 30\%$. With smaller variations in the energy barrier, the finite-T strength would thus deviate

by a similar ±30%. The full predictions here are generally in much better agreement with experiment, although requiring far greater computational cost. We will report on results of such an analysis for the Cu-Mn and Cu-Ge systems, providing a different interpretation of the data in Ref. [17], in a future publication. Such a strategy is similar in spirit to the work of Zander *et al.* [34, 35] who computed $\Delta v_m^{(i)}$ for various solutes using first-principles and then assumed $\sigma_y = K \sum_i c_i^{2/3} \Delta v_m^{(i)4/3}$, with K as a single fitting parameter independent of solute. However, our analysis here shows that the additivity assumed by Zander *et al.* should be replaced by Eq. (2.38). We provide additional insight into the energy barrier so that the results can be applied at finite temperature, although Eq. (2.40) shows such an approach to only have reasonable accuracy.

The overall methodology presented here, including the full first-principles analysis of the solute/dislocation core interactions and validated for Al-X alloys, is robust and can readily be applied to other fcc alloys as well as basal slip in hcp alloys. We will report on application of the model to basal slip in Mg-Al in the next chapter. This model thus represents a significant advance in computational metallurgy that can be used to guide the design of technologically important multicomponent solute strengthened alloys.

Chapter 3

Solute strengthening in Mg-Al alloys from first-principles

3.1 Introduction

Interest in using magnesium alloys as structural materials has been increasing due to their excellent material properties, such as low density and high specific strength [51, 52]. In particular, applications of magnesium alloys to the automotive industry looks promising due to the ever increasing demand for more light weight, fuel-efficient vehicles [53]. However, limitations in formability prevent the wide-spread adoption of magnesium alloys. This limitation stems from the anisotropy in plasticity response associated with the various dislocation slip systems in the hexagonal close packed (hcp) structure. Processing and alloying strategies are aimed at overcoming these limitations, and these

strategies can be informed through a detailed understanding of the deformation mechanisms occurring in Mg and its alloys.

Advancements in computational capabilities have enable the study of disocation structure and mobility mechanisms. Molecular dynamics has been use to study dislocation [54–60] and twin [61–63] structures in magnesium. However, the predicted behavior depends strongly on the interatomic potentials used so that such studies have limited predictive capability, and the availability of potentials for alloy systems is limited. First-principles calculations have emerged to examine some dislocation core structures and energetics [4, 6, 64–66]. However, dislocations such as $\langle c+a \rangle$ have a large burgers vector and MD studies suggest that the cores are spread considerably, making first-principles modeling computationally challenging. Extending first-principles studies to direct modeling of dislocation motion or core structural changes upon alloying, for instance, remains prohibitive in most cases. Thus, despite notable advancements, predictions for important quantities such as the finite temperature yield stress of an alloy do not yet exist.

In this chapter, we advance the field by using first-principles energetics of solutes in and around the basal dislocation core as input to an analytic model for solute strengthening, from which we make parameter-free predictions of the yield stress versus temperature for basal slip in Mg-Al alloys. Our predictions are in excellent agreement with literature experimental data over a range of Al concentration. The main feature of the work is our use of a new model for solute strengthening that has been successfully applied to Al-X alloys [37, 67] with the first-principles input coming from Yasi et al. [4]. While the quantitative success is impressive, a new physical feature of Mg-Al also emerges naturally from the theory. Specifically, because the dissociation of the basal edge core into partials

is wider than in Al, the theory predicts the existence of two possible energetically stable dislocation configurations. One configuration has a low energy barrier but a high zero-temperature flow stress while the other configuration has a high energy barrier but a low zero-temperature flow stress. Considering both configurations, the flow stress is controlled by the first configuration at low temperature and the second configuration at high temperature. The flow stress versus temperature thus shows a high-temperature domain that is relatively temperature-insensitive and appears similar to an "athermal" strength. Such an "athermal" regime is often observed in many materials [5, 17, 21, 68–75] and is usually attributed to unquantified "long-range" dislocation interactions. Our theory demonstrates that this apparent "athermal" regime remains quantitatively attributable to the solute strengthening and predicts the variation of this "athermal" regime as a function of Al solute content in good agreement with data. This chapter is limited to the study of Al solutes effects on basal slip in Mg, but the concepts are readily extended to other solutes and dislocation types. Moreover, our study demonstrates that a steady insistence on mechanistic details based on computable material quantities pays dividends in the form of both quantitative results and new physical insights.

3.2 Solute Strengthening Model

The solute strengthening model is described in detail in Ref. [37, 67]. The model uses concepts first developed by Labusch [13, 15] but introduces key modifications that render the model convergent and parameter-free. The key concept in the model is that an initially straight dislocation in a random field of solutes can lower its energy by seeking out regions in the solid containing favorable solute fluctuations. The dislocation

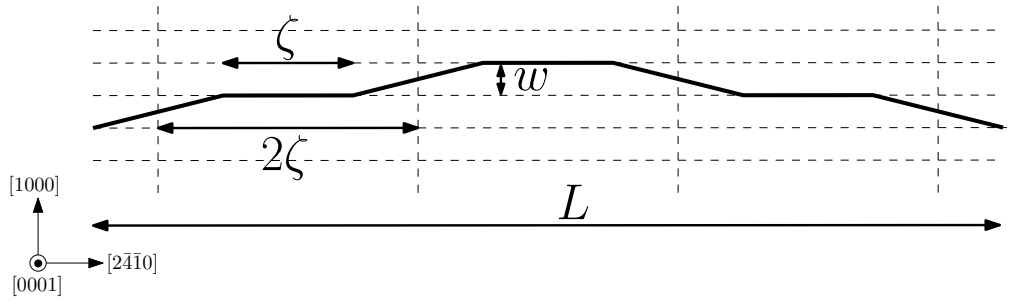

FIGURE 3.1: Schematic of a dislocation roughening into segments of length 2ζ over length w due to favorable solute fluctuations.

accomplishes this by bowing out towards these favorable fluctuations. While the bowed out segments lower their interaction energy with the solutes, the bowing out process increases the line energy of the dislocation. The total change in energy as the dislocation goes from the straight configuration to the bowed out configuration is therefore the sum of the contribution due to favorable solute fluctuations and the elastic energy cost of bowing out.

We consider a positive basal edge dislocation of length L lying in the $z-$direction, with Burgers vector b in the $x-$direction and evaluate the total energy of a fluctuating configuration shown schematically in Figure 3.1, where straight dislocation segments of length ζ lie in regions of favorable solute fluctuations, with bowing out of amplitude w and intermediate segments of length ζ connecting these segments to form the overall dislocation line. The interaction energies between solutes and the dislocation are obtained through first-principles computations. We minimize the total energy of the dislocation to find the characteristic scales ζ_c and w_c as a function of the interaction energies, dislocation line tension, solute concentration, and other material parameters.

We now sketch out the path from solute/dislocation energies to dislocation strengthening; a full description is provided in Ref. [67]. A key quantity in the analysis is the

potential energy decrease due to favorable solute fluctuations, which is obtained by considering the standard deviation of the total solute/dislocation interaction energy as the dislocation segment of length ζ moves a distance w from its original position,

$$\Delta E_p(\zeta, w) = -\left[\left(\frac{c\zeta}{\sqrt{3}b}\right)^{\frac{1}{2}} \Delta\tilde{E}_p(w)\right] \cdot \left(\frac{L}{2\zeta}\right) \tag{3.1}$$

where

$$\Delta\tilde{E}_p(w) = \left[2\sum_{ij}\left(1-\chi(w, y_j)\right) U(x_i, y_j)^2\right]^{\frac{1}{2}}, \tag{3.2}$$

Here, $U(x_i, y_j)$ is the solute/dislocation interaction energy of a solute at position (x_i, y_j, z) with a dislocation centered at the origin and

$$\chi(w, y_j) = \frac{\sum_k U(x_k - w, y_j)\, U(x_k, y_j)}{\sum_k U(x_k, y_j)^2}. \tag{3.3}$$

is the correlation function of the solutes in the y_j^{th} layer when the dislocation segment moves a distance w. The total energy change as the dislocation goes from the straight configuration to the one depicted in Figure 3.1 is then

$$\Delta E_{tot}(\zeta, w) = \left[\left(\Gamma\frac{w^2}{2\zeta}\right) - \left(\frac{c\zeta}{\sqrt{3}b}\right)^{\frac{1}{2}} \Delta\tilde{E}_p(w)\right] \cdot \left(\frac{L}{2\zeta}\right). \tag{3.4}$$

Minimizing Eq. (3.4) with respect to ζ yields the characteristic segment length ζ_c as a function of the roughening amplitude w,

$$\zeta_c(w) = \left(4\sqrt{3}\frac{\Gamma^2 w^4 b}{c\Delta\tilde{E}_p^2(w)}\right)^{\frac{1}{3}}, \tag{3.5}$$

and the total energy change ΔE_{tot}

$$\Delta E_{tot}\left(w, \zeta_c\left(w\right)\right) = -\frac{3^{2/3}}{8\ 2^{1/3}}\left(\frac{c^2 \Delta \tilde{E}_p^4\left(w\right)}{b^2 w^2 \Gamma}\right)^{\frac{1}{3}} L. \tag{3.6}$$

as a function of only w. Numerical minimization of the total energy per unit length $\Delta E_{tot}/L$ gives the characteristic roughening amplitude w_c. The associated characteristic energy ΔE_c of each "unit cell" of dislocation line consisting of the straight segment of length ζ_c and the surrounding segment length of $zeta_c$ is then given by

$$\Delta E_c = \frac{3^{5/6}}{2^{5/3}}\left(\frac{c w_c^2 \Gamma \Delta \tilde{E}_p^2(w_c)}{b}\right)^{\frac{1}{3}}. \tag{3.7}$$

The zero-temperature energy barrier for motion of the dislocation is the average energy change as the dislocation segment moves from some favorable *minimum* to a maximum w_c, which can be shown to be [37],

$$\Delta E_{b,i} = \left(\frac{4\sqrt{2}-1}{3}\cdot\frac{3^{5/6}}{2^{5/3}}\right)\left(\frac{c w_{c,i}^2 \Gamma \Delta \tilde{E}_p^2(w_{c,i})}{b}\right)^{\frac{1}{3}}. \tag{3.8}$$

The finite-temperature flow behavior follows from standard thermal-activation theory with the energy barrier computed above plus considerations from Labusch regarding larger-scale fluctuations of the dislocation configuration that can arise with increasing temperature (corresponding to lower applied stresses). Under an applied resolved shear

stress τ, the energy barrier can be approximated by

$$\Delta E(\tau) = \begin{cases} 0.51\ \Delta E_b \log\left(\frac{\tau_{y0}}{\tau}\right), & \tau/\tau_{y0} < 0.46 \\ \Delta E_b \left[1 - \left(\frac{\tau}{\tau_{y0}}\right)\right]^{\frac{3}{2}}, & \tau/\tau_{y0} \geq 0.46 \end{cases} \tag{3.9}$$

where τ_{y0} is the zero temperature yield stress,

$$\tau_{y0} = 1.01 \cdot \left(\frac{c^2 \Delta \tilde{E}_p^4(w_c)}{\Gamma b^5 w_c^5}\right)^{\frac{1}{3}}. \tag{3.10}$$

Once again, using the same arguments as that stated in Section 1.4, the finite temperature stress required for dislocation flow is given by

$$\tau_y(T) = \begin{cases} \tau_{y0} \exp\left(-\frac{1}{0.51}\frac{kT}{\Delta E_b} \ln \frac{\dot{\epsilon_o}}{\dot{\epsilon}}\right) & \tau/\tau_{y0} < 0.46 \\ \tau_{y0}\left[1 - \left(\frac{kT}{\Delta E_b} \ln \frac{\dot{\epsilon_o}}{\dot{\epsilon}}\right)^{\frac{2}{3}}\right] & \tau/\tau_{y0} \geq 0.46 \end{cases} \tag{3.11}$$

3.3 Solute/dislocation Interaction Energies

To evaluate Eq. (3.1), accurate determination of $U(x_i, y_j)$ is essential. Far from the dislocation core, the continuum approximation

$$U(x_i, y_j) \approx -p(x_i, y_j)\,\Delta v \tag{3.12}$$

is accurate, where Δv is the misfit volume of the solute and $p = -\sigma_{kk}/3$ is the pressure field exerted by the dislocation at the location of the solute [7]. The misfit volume is

calculated using Density Functional Theory (DFT), implemented through *Vienna Ab-initio Simulations Package* (VASP) using a methodology described in Ref. [37], and is determined to be $\Delta v = -7.89$ Å^3. The pressure field $p(x_i, y_j)$ is calculated using the Peierls-Nabarro model,

$$p(x_i, y_j) = -\frac{1-\nu}{1+\nu}\frac{\mu}{3\pi}\int_{-\infty}^{\infty}\frac{b'(x')\ y_j}{(x_i - x')^2 + y_j^2}dx' \tag{3.13}$$

where ν is the Poisson ratio and μ is the shear modulus of magnesium. The distribution of the Burgers vector $b'(x') = db/dx$ is calculated using the first-principles-computed dislocation core structure from Ref. [4] that is shown in Figure 3.2(a). This structure is obtained through the use of a DFT domain that is coupled with a Lattice Green's Function method to simulate an isolated dislocation in an infinite solid.

Near the dislocation partials, the deformation is very large and the continuum approximation is not accurate, necessitating the first-principles computations. The DFT results of Yasi *et al.* in this core region are shown in Figure 3.2(a) and shows that the DFT results must be used for atomic sites in the two rows above the slip plane and in one row below the slip plane. The DFT data does not extend laterally outside the core and also does not include all sites within the core. We thus use the DFT data and cubic splines to interpolate the energies at sites along each atomic plane while enforcing convergence to the continuum results far to the left and right of the core. The solute/dislocation interaction energies so obtained are shown in Figure 3.2(a), matching the DFT data and smoothly merging into the continuum results outside the core.

With the interaction energies established, we can compute the correlation function

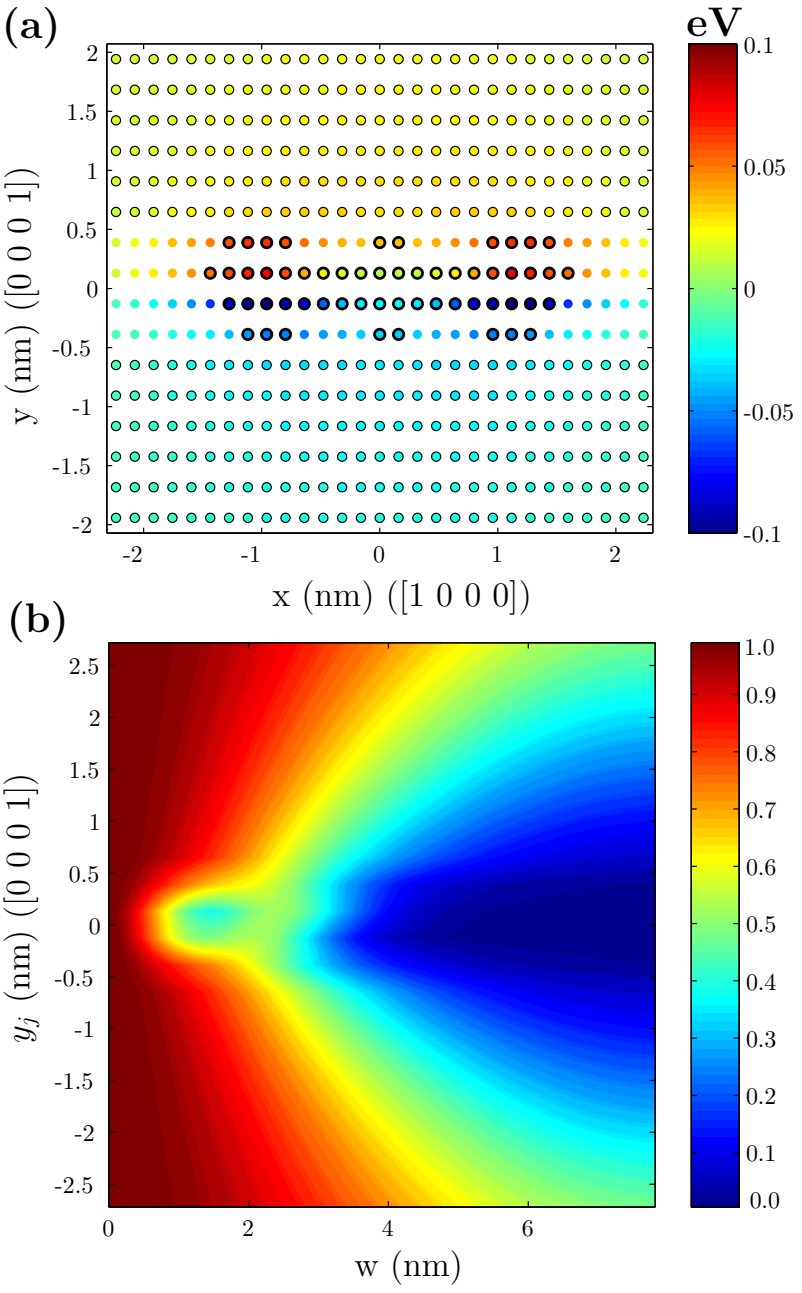

FIGURE 3.2: (a) Solute/dislocation interaction energy map for Al solutes as a function of solute position. Circles with bold outline are from Ref. [4]; cicles with non-bold outline are from Eq. (3.12); cicles with no outline are interpolated using cubic splines. (b) A contour plot of the correlation function $\chi(w, y_j)$ for a solute initially $(0, y_j)$ as the dislocation moves a distance w away, as computed for an Mg-Al alloy.

$\chi(w, y_j)$, which reflects how the interaction energy of a solute on a particular atomic plane parallel to the slip plane is correlated as the dislocation slides by on the slip plane. This correlation function is shown in Figure 3.2(b), and shows that the solutes immediately in the partials are decorrelated when the dislocation has moved by one-half the partial separation distance, and then are slightly more correlated as the dislocation moves by another one-half of the partial separation, followed by a rapid decay in the correlation. In contrast, solutes in atom planes further from the slip plane are highly correlated over much longer distances, with even the first few planes reasonably correlated over distances of the order of $3nm$. These differences in correlation of the solute energies will be shown below to have an important effect on the overall dislocation configurations and energetics, and subsequently the finite-temperature flow stress.

3.4 Predictions and Discussion

Using the energies and correlation function shown in Figures 3.2(a) and 3.2(b), we can compute the dislocation energy per unit length as a function of the amplitude w of the fluctuations (Eq. (3.6)) and look for the value w_c that minimizes the energy. In the calculations, we use the line tension $\Gamma = 4.0$ eV/nm [50]. Figure 3.3 demonstrates that for Mg-Al there are two minima, not just one as in Al, corresponding to two roughening amplitudes $w_{c,1}$ and $w_{c,2}$, and two associated segment lengths $\zeta_{c,1}$ and $\zeta_{c,2}$ and characteristic energy barriers $\Delta E_{b,1}$ and $\Delta E_{b,2}$.

The two minima arise because of the nature of the correlations in the interaction energies. Due to the large partial separation in Mg basal edge dislocations, moving the dislocation

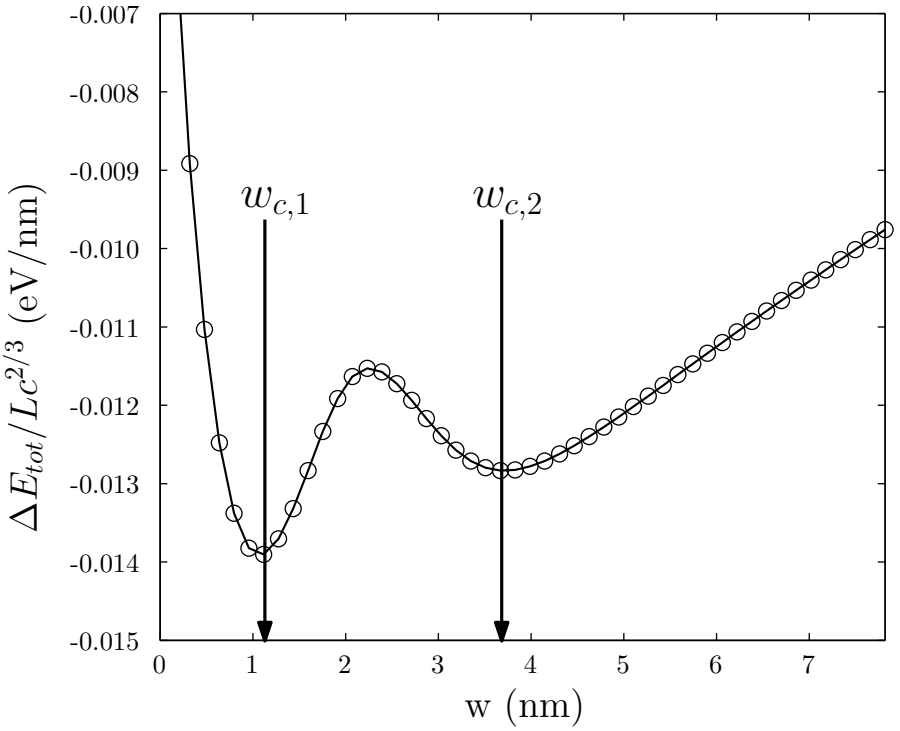

FIGURE 3.3: Normalized energy per unit length $\Delta E_{tot}/Lc^{2/3}$ versus roughening amplitude w for an Mg-Al alloy.

by $w_{c,1} = 0.98$ nm almost completely decorrelates the solute fluctuations within the partials of the dislocation ($|y_j| \leq 2$), resulting in the first minimum. However, this small roughening amplitude is not sufficient to the decorrelate solutes farther from the dislocation core ($|y_j| > 2$). By increasing the roughening amplitude, the dislocation is able to access favorable fluctuations far away from the core, leading to the second minimum at $w_{c,2} = 3.67$ nm. In Al, which has a smaller partial dissociation distance, only one minimum exists. Thus, we see that the detailed structure of the dislocation core, which is accurately predicted only by first-principles methods, plays a key role in determining the characteristic length and energy scales for solute strengthening.

The values for w_c, ζ_c, and ΔE_b for the two minimizing configurations 1 and 2 are shown in Table 3.1. Configuration 1, associated with the near-core behavior, has a relatively

TABLE 3.1: Parameters for the two dislocation configurations in Mg-Al alloys, normalized by the appropriate scaling of the solute concentration.

Normalized Parameter	**Config. 1**	**Config. 2**
w_c	1.12 nm	3.67 nm
$\zeta_c \cdot c^{1/3}$	6.04 nm	20.66 nm
$\Delta E_b/c^{1/3}$	1.92 eV	6.07 eV
$\tau_{y0}/c^{2/3}$	224.4 MPa	63.0 MPa

higher zero temperature yield stress but a relatively low energy barrier. Configuration 2, associated with the longer-range fluctuations, has a lower zero temperature yield stress but exhibits a higher energy barrier. The effect on the finite-temperature yield strength is that the dislocation can sample both configurations, and so must overcome both via thermal activation to achieve glide. The strain rate $\dot{\epsilon}$ as a function of stress and temperature is thus given by

$$\frac{1}{\dot{\epsilon}} = \frac{1}{\dot{\epsilon_1}} + \frac{1}{\dot{\epsilon_2}} = \frac{1}{\dot{\epsilon}_\circ}\left[\exp\left(\frac{\Delta E_1\left(\tau\right)}{kT}\right) + \exp\left(\frac{\Delta E_2\left(\tau\right)}{kT}\right)\right]. \tag{3.14}$$

Inverting Eq. (3.14) gives the finite temperature yield stress $\tau_y\left(T, \dot{\epsilon}\right)$ of the alloy. Physically, the two configurations control different stress/temperature regimes of the flow behavior. At low stresses/high temperatures, since $\Delta E_1 < \Delta E_2$ then $\dot{\epsilon}_2 \ll \dot{\epsilon}_1$ and $\dot{\epsilon} \approx \dot{\epsilon}_2$; the temperature is sufficiently high such that the dislocation is easily thermally activated over the smaller ΔE_1 barriers and the larger ΔE_2 barrier controls the thermal activation. Conversely, at high stresses/low temperatures, $\Delta E_2 < \Delta E_1$, and $\dot{\epsilon}_1 \ll \dot{\epsilon}_2$, so that $\dot{\epsilon} \approx \dot{\epsilon}_1$; the stress is sufficiently high to suppress the longer-range barrier of configuration 2, leaving the barrier ΔE_1 to control the thermal activation.

The analytical prediction of the existence of two different minimum configurations, corresponding to two different energy barriers at two different length scales, is unexpected.

To validate this result further, we thus performed direct stochastic simulations of straight dislocation segments moving through a random field of solutes. In this case the value of ζ is fixed but the presence of the solute correlations should still reveal the existence of two energy barriers that control the flow in different regimes of stress. The simulation is performed as follows. The total solute/dislocation interaction energy is calculated as a function of the dislocation segment glide position x. The dislocation is then placed at one of the many local energy minima and the largest energy barrier ahead of the dislocation is recorded, but restricting to a distance $2w_{c,2}$ to avoid very long-range barriers that are irrelevant. An increasing applied stress is then imposed on the system and the barrier height versus stress is measured, generating a simulated $\Delta E(\tau)$. This process is repeated 3000 times to get statistically significant results. The analytic model predicts two barriers that should vary as

$$\Delta E_i'(\tau,\zeta) = \Delta E_{b,i}' \left[1 - \frac{\tau}{\tau_{y0,i}'(\zeta)}\right]^{\frac{3}{2}}, \tag{3.15}$$

with

$$\tau_{y0,i}'(\zeta) = \frac{\pi}{2}\frac{\Delta E_{b,i}'(\zeta)}{b\zeta w_{c,i}}. \tag{3.16}$$

where the prime (') indicates that these predictions are based only on the potential energy, since elastic effects of bowing are not included. The theory also shows that the energy barrier should scale as $\zeta^{1/2}$ and the strength should scale as $\zeta^{-1/2}$, so we plot $\Delta E\zeta^{-1/2}$ vs. $\tau\zeta^{1/2}$ to obtain results independent of the actual ζ. The simulated energy barrier vs. stress and the predictions of the analytical model are shown in Figure 3.4(a), and show precisely the behavior anticipated in the discussion above. At low stresses, the longer-range fluctuations with the larger energy barrier $\Delta E_2'$ persist and control the

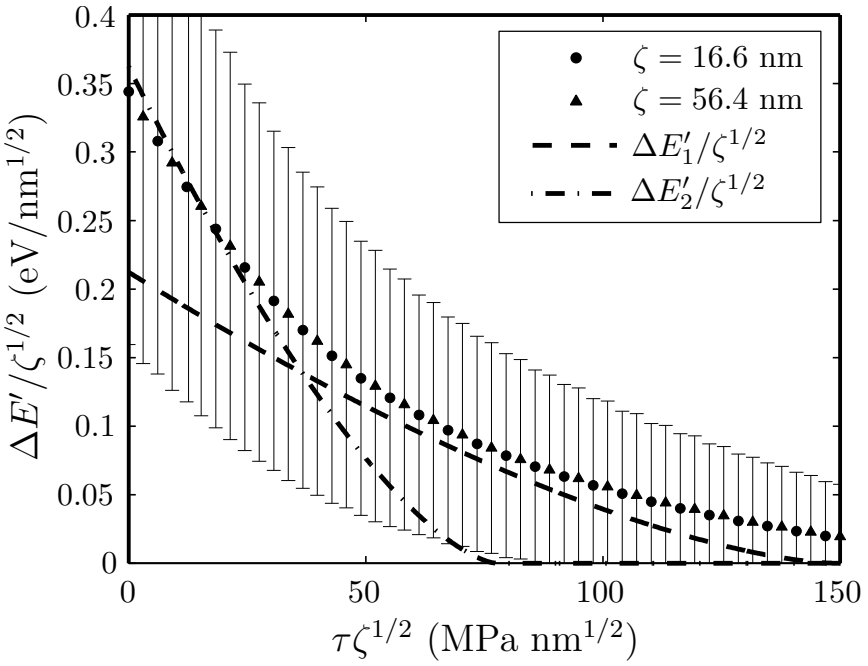

FIGURE 3.4: Comparison between the stress dependent energy barrier $\Delta E'(\tau)$ determined using the direct stochastic simulation and that expected by the analytic model for a dislocation segment of length $\zeta = 16.6$ nm and $\zeta = 56.4$ nm.

overall energy barrier. At high stresses the long-range barriers are defeated and the short-range barriers persist and control the overall energy barrier. The stochastic simulations thus validate the existence of two different energy barriers, with two different length scales and zero-temperature yield stresses, and show that two corresponding regimes of flow behavior exist.

We now compare predictions of the model against experimental data. The critical resolved shear stress (CRSS) $\tau_{y,expt}^{Mg-Al}$ for basal slip in a range of Mg-Al alloys over a range of temperatures was measured at a strain rate of $\dot{\epsilon} = 1.66 \times 10^{-4}$ s^{-1} by Akhtar and Teghtsoonian [5]. They also measured the CRSS $tau_{y,expt}^{Mg}$ for pure Mg, i.e. the Peierls barrier, at the same temperatures. Because the alloy strengths are not significantly larger than the Peierls stress for pure Mg, it is necessary to include the Peierls stress

along with the solute-strengthening prediction. Because the Peierls barrier is associated with slip over one burgers vector while the solute strengthening is associated with slip over the larger length scales w_c, it is appropriate to add the two contributions to obtain the total strength. Our prediction is thus

$$\tau_y = \tau_{y,expt}^{Mg} + \tau_{y,theory}^{Mg-Al} \tag{3.17}$$

where $\tau_{y,theory}^{Mg-Al}$ is computed using our theory. In the predictions, we use $\dot{\epsilon}_\circ = 10^5$ but the results depend very weakly on the precise since it appears in the logarithm in Eq. (3.11). Figure 3.5(a) shows the yield stress τ_y of three different Mg-Al alloys at various temperatures and as predicted by our model. The agreement is extremely good over the entire range of concentrations and temperatures, with no fitting or adjustable parameters whatsoever. Figure 3.5(b) shows the experimental results versus the predictions; all of the materials cluster along a line of slope unity that indicates perfect agreement.

We note that the predictions nicely capture the transition in strength with increasing temperature, where the experimental data appears to approach a "plateau". Such a plateau, widely seen in solute-strengthened materials, is often ascribed to some long range, internal stresses that contribute some "athermal" strengthening due to some other mechanism, e.g. solute multiplets [17], elastic dislocation/dislocation interactions [76], or solute drag "friction" [21], but without quantitative analysis or prediction [11]. Other workers, attempting to explain the solute-concentration dependence of the plateau, have invoked the standard solute-strengthening theories themselves to predict the plateau, leaving open the origins of the lower-temperature strengthening [17, 69, 73, 74, 77, 78] and are still quantitatively lacking.

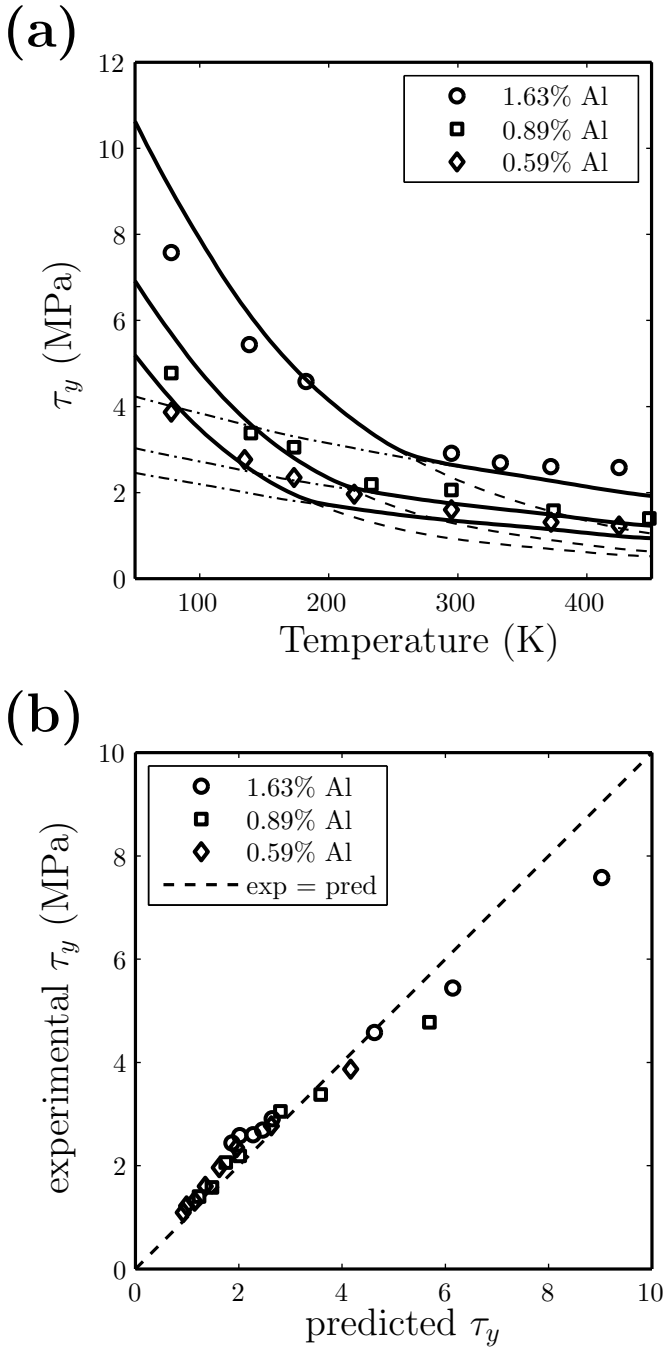

FIGURE 3.5: (a) Experimental [5] and predicted finite temperature yield stress $\tau_y(T)$ for three different Mg-Al alloys. The solid lines are $\tau_{y,\text{eff}}$, the dashed lines are τ_{y1} and the dashed-dot lines are τ_{y2}. (b) Experimental versus predicted yield stress τ_y for the three alloys presented above. The dashed line has a slope of unity and indicates perfect agreement.

In contrast, the present theory, based on a sound mechanistic analysis and the most accurate computations currently possible, reveals a physical origin for this athermal stress. We find that the "plateau" is indeed directly connected to the solute strengthening itself, but physically due to the wide dissociation of the dislocation core structure that leads to correlations in solute/dislocation interactions over a longer length scale than just the core itself. The higher energy barrier $\Delta E_{c,2}$ over a longer range ($w_{c,2}$ leads to a much weaker dependence of strength versus temperature in the higher temperature regime than in the low temperature regime. At the same time, the short-range solute correlations are responsible for the low-temperature strengthening. We postulate that the mechanism observed here for Mg is a general one that operates for materials with a large partial spacing, the latter arising in materials with a low stable stacking fault energy. And indeed, the material systems where a concentration-dependent "athermal" "plateau" stress is observed are those with low stacking fault energies: Cu[17, 21, 71–75], Ag[21, 70, 73], and Au[69] alloys. Thus, no new mechanisms are required to explain the high-temperature behavior in Mg and the explanation for Mg is qualitatively consistent with trends in other materials.

3.5 Conclusion

We have applied the parameter-free solute strengthening model of Ref [37] to accurately predict the finite temperature basal flow stresses of Mg-Al alloys, using first-principles data on solute/dislocation interactions from the work of Yasi *et al.*[4]. This demonstrates that the model, previously applied to Al-X alloys, has broader applicability to materials where solute effects are limited to influencing the glide along the slip plane. In the

case of Mg, the dissociated nature of basal edge dislocation has consequences for solute strengthening that are absent from the case of Al-X alloys. Specifically, the broader core spreading leads to two different possible minimum energy configurations for the dislocation, leading ultimately to a transition in the controlling configuration as the temperature is increased. This transition is manifested in an apparent plateau in the strength vs. temperature at higher temperatures. Overall, our results demonstrate that an insistence on rigorous mechanistic modeling, with accurate first-principles input, pays high dividends in achieving predictive models that, moreover, can reveal new mechanisms of material behavior that has previously evaded explanation.

Chapter 4

Strong-/weak-pinning transition at finite temperature

4.1 Introduction

Solute strengthened alloys are some of the most technologically important materials in industry. Understanding the strengthening mechanisms in solid solutions is therefore important for developing accurate constitutive models used to design components and, moreover, to design new alloys with improved processing. The fundamental physical origin of solute strengthening is the interaction between the dislocation deformation, e.g. the stress field, and the solute deformation, e.g. the distortional strain it creates when introduced into a substitional lattice site. Due to this interaction, dislocation motion under an applied shear stress is suppressed, leading to an increase in the alloy yield stress with increasing solute concentration. However, since the dislocation can interact

with many solutes (on, above, and below) the glide plane and since the dislocation is a flexible line, the actual strengthening depends on the configurations the dislocation takes within the random field of solutes.

There are two broad classes of theories for solute strengthening. The strong-pinning theory (Friedel [8], Fleischer [7, 9]) considers the solute atoms in the plane of the dislocation as independent point obstacles that pin the dislocation, which bows out in the regions between the solutes. With the parameter f_{max} characterizing the solute's maximum resistive force, the zero temperature yield stress for the Friedel mechanism, τ_{y0}^{F}, corresponds to the stress required to bow out the dislocation line in between the pinning solutes sufficiently to overcome their resistive force, leading to

$$\tau_{y0}^{F} = \frac{f_{max}}{b\zeta_F\left(\tau_{y0}^{F}\right)} = \left(\frac{f_{max}}{2\Gamma}\right)^{\frac{3}{2}}\left(\frac{2\Gamma}{b^2}\right)c^{\frac{1}{2}}. \tag{4.1}$$

where ζ_F is the Friedel sampling length and Γ is the dislocation line tension.

The weak-pinning model (Mott [14] and Labusch [13, 15]) considers the collective interaction of many solutes around the dislocation, and attributes strengthening to the occurence of favorable statistical fluctuations in the solute configuration, when each individual solute alone would not be strong enough to pin the dislocation at the same stress level. Labusch first developed a model for considering solutes in the glide plane of the dislocation, although the concept is really three-dimensional in nature. Labusch derived a zero-temperature flow stress uses many of the same parameters as in the Friedel model plus a parameter w capturing the spatial range of interaction of the solutes with the

dislocation. The zero-temperature Labusch strength in this case is given by

$$\tau_{y0}^{L} = \left(\frac{c^2 U_{max}^4}{w \Gamma b^9} \right)^{\frac{1}{3}}. \tag{4.2}$$

where U_{max} is the maximum solute/dislocation interaction energy.

Using the zero-temperature results above, the transition between the two can be made by assuming that the strongest of the two mechanisms is operative. By taking the ratio of the Friedel strength to the Labusch strength, we obtain the condition

$$\frac{\tau_{y0}^{F}}{\tau_{y0,L}} \propto \left(\frac{f_{max} b^2}{\Gamma c w^2} \right)^{\frac{1}{6}}. \tag{4.3}$$

This ratio is essentially the β parameter first identified by Labusch,

$$\beta = \frac{f_{max} b^2}{4 \Gamma c w^2} \tag{4.4}$$

although the analysis followed a different path. For a given solute, all material parameters are unchanged, so that the transition occurs at a solute concentration $c_\circ$ given by

$$c_\circ = \frac{f_{max} b^2}{4 \Gamma w^2}. \tag{4.5}$$

Using typical material properties (see below for more details), the Friedel model should be applicable at concentrations below $\sim 10^{-2}$. Thus, it is often assumed that the Friedel model is applicable for dilute alloys. However, this result is based on zero-temperature considerations and a restricted version of the Labusch concept for "weak" pinning. It is the flow stresses at finite temperatures and finite strain rates that are experimentally

relevant, and the transition should be based on a Labusch-type model that includes solutes off the glide plane.

Since all of the necessary material parameters to assess the two models were not available, and neither model could quantitatively predict alloy strengthening (although trends and scaling could be identified), the domains of applicability of the two models were not of great importance. In recent years, the ability to obtain dislocation/solute interaction energies using first-principles quantum mechanical methods, and the creation of a new predictive model for the Labusch regime, has overcome these limitations. A clear delineation of the domains of dominance of the Labusch-like and Friedel pinning models, including at finite temperature, thus has new relevance for understanding and designing solute-strengthened metals. The purpose of this chapter is to examine this transition in detail, using parametric studies that span a wide range of possible dislocation structure and highly-accurate studies that use first-principles data for solutes in Al alloys. We show that over a wide range of dislocation structures, and specifically for Al alloys and basal/prism slip in Mg alloys, that the Labusch-type model controls that strength over a wide range of temperatures and at atomic solute concentrations higher than 10^{-4}. Thus, contrary to the conventional wisdom of the zero-temperature transition condition given by Eqn. (4.4), the Friedel model has very limited applicability, and the Labusch model should be the prevailing model for solute strengthening across a wide class of metals.

The remainder of this chapter is organized as follows. In Section 4.2, we briefly discuss thermally-activated flow, leading to the finite-temperature, finite-strain rate flow stress, for the Friedel model. We then present the results of our recent predictive Labusch-type model for finite-temperature flow stress [37, 67]. In Section 4.3 we use an analytic

Peierls-Nabarro-type model to generate the dislocation/solute interaction energies for dislocation cores of varying degrees of dissociation and partial spreading, and examine the Friedel-Labusch transition quantitatively. In Section 4.4, we use first-principles dislocation/solute interaction energies for Al-X (X = Mg, Si, Cu, Cr, Mn and Fe) and Mg-Al alloys to make specific predictions for the Friedel-Labusch transition as a function of temperature and solute concentration. These results show that the Labusch-type model is dominant over nearly the entire practical range of temperatures ($T > 78K$) and solute concentrations ($c > 10^{-5}$) in these materials systems. In Section 4.5 we discuss some additional considerations and summarize.

4.2 Finite-Temperature Friedel and Labusch-type Models

At finite temperature, the dislocation can pass an individual solute via thermal activation over the energy barrier imposed by the solute atom at any applied stress τ less than the zero temperature yield stress τ_{y0} [21]. The stress-dependent energy barrier $\Delta E^F(\tau)$, including the effects of bowing that relate the applied stress to the force on the solute, follows the general form

$$\Delta E^F(\tau) = E_{max}\left[1 - \left(\frac{\tau}{\tau_{y0}^F}\right)^p\right]^q \tag{4.6}$$

where E_{max} is the maximum solute/dislocation interaction energy and the parameters $0 < p < 1$ and $1 < q < 2$ depend on the details of the force-distance profile of the solute obstacle [12]. A representative case is $p = 2/3$ and $q = 3/2$ corresponding to a

parabolic force-distance profile [20]. Other profiles can be considered [17], but this does not significantly change the conclusions of this chapter.

For a quasistatic loading, the rate of escape ν by activation over the stress-dependent barrier height $\Delta E^F(\tau)$ can be approximated using transition state theory [21] as $\nu = \nu_\circ \exp(-\Delta E^F(\tau)/kT)$ where $\nu_\circ$ is the attempt frequency, T is the temperature, and k is Boltzmann's constant. The microscopic dislocation escape rate ν can be related to the macroscopic strain rate $\dot{\epsilon}$ by the well established model [12],

$$\dot{\epsilon} = \dot{\epsilon}_\circ \exp\left(-\frac{\Delta E^F(\tau)}{kT}\right) \tag{4.7}$$

where $\dot{\epsilon}_\circ = \rho b d \nu_\circ$ is the reference strain rate, ρ is the dislocation density per unit area and d is the flight distance over which the dislocation moves after each escape. This relation, along with Eq. (4.6), can be inverted to obtain the finite temperature stress required for dislocation flow as

$$\tau_y^F(T, \dot{\epsilon}) = \tau_{y0}^F \left[1 - \left(\frac{T}{T_\circ^F}\right)^{\frac{2}{3}}\right]^{\frac{3}{2}} \tag{4.8}$$

where $T_\circ^F = E_{max}/k \ln(\dot{\epsilon}_\circ/\dot{\epsilon})$ is the characteristic temperature for the Friedel mechanism. The Friedel model is thus characterized by two key features of the dislocation/solute interaction: the energy barrier E_{max} and the maximum force f_{max}, which corresponds to the maximum slope of the interaction energy versus solute/dislocatoin distance along the glide plane.

In the Labusch-type model, an initially-straight dislocation is allowed to bow in the glide plane to seek out favorable local environments of the random solutes that minimize the

potential energy. The bowing has a cost in elastic energy, and so the typical configuration of the dislocation is that which minimizes the total energy as a function of the wavelength ζ and amplitude w of the bowing. We have recently developed a model based on this general physical picture in Refs. [37, 67] that includes the finite-temperature flow stress. The outcomes of our analysis are a characteristic wavelength ζ_c and amplitude w_c, and an associated energy barrier ΔE_b and zero-temperature flow stress τ_{y0}^L. These quantities are given by

$$\zeta_c\left(w\right) = \left(4\sqrt{3}\frac{\Gamma^2 w_c^4 b}{c\Delta\tilde{E}_p^2(w_c)}\right)^{\frac{1}{3}}, \tag{4.9}$$

$$\Delta E_b = \left(\frac{4\sqrt{2}-1}{3}\cdot\frac{3^{5/6}}{2^{5/3}}\right)\left(\frac{cw_c^2\Gamma\Delta\tilde{E}_p^2(w_c)}{b}\right)^{\frac{1}{3}}. \tag{4.10}$$

and

$$\tau_{y0}^L = 1.01\cdot\left(\frac{\Delta\tilde{E}_p^4(w_c)}{\Gamma b^5 w_c^5}\right)^{\frac{1}{3}} c^{\frac{2}{3}}. \tag{4.11}$$

where

$$\Delta\tilde{E}_p\left(w_c\right) = \left[2\sum_{ij}\left(1-\chi\left(w_c,y_j\right)\right)U\left(x_i,y_j\right)^2\right]^{\frac{1}{2}}, \tag{4.12}$$

and $U(x_i, y_j)$ is the interaction energy between a solute at position (x_i, y_j) relative to a dislocation centered at the origin and

$$\chi\left(w,y_j\right) = \frac{\sum_k U\left(x_k-w,y_j\right)U\left(x_k,y_j\right)}{\sum_k U\left(x_k,y_j\right)^2}. \tag{4.13}$$

is the correlation function of that interaction energy as the dislocation glides from one location to another location a distance w away. The characteristic quantity w_c is computed by minimization of the total energy, and so is not expressible in an analytic form. We note that this formulation includes the dislocation/solute interactions throughout

all space. It is through the correlation function of this energy that the sums in the formulation become convergent, because U scales only as $1/r$ for large distances r, and so the formulation is rather different than the nominal Labusch model. Physically, the length w_c seems similar to the "range of the solute/dislocation interaction w" in the original Labusch model. but we will see below that w_c and w enter rather differently in the predicted transition from weak to strong pinning.

The thermally-activated behavior for this Labusch-type model follows arguments similar to those for the Friedel model with the stress-dependent energy barrier taking the form of Eq. (4.6) with $p = 1$ and $q = 3/2$,

$$\Delta E^L(\tau) = \Delta E_b \left[1 - \left(\frac{\tau}{\tau_{y0}^L}\right)\right]^{\frac{3}{2}}, \tag{4.14}$$

At elevated temperatures, Eq. (4.14) actually transitions over to an logarithmic form, as discussed by Labusch [79]. This means the Labusch mechanism becomes more dominant than predicted by Eq. (4.14) with increasing temperature. However, the temperature range at which the logarithmic form is relevant in the Friedel-Labusch transition is narrow, occurs at very low concentrations ($< 10^{-5}$), and Eq. (4.14) is assumed to apply for $T < T_\circ^F$ and this assumption has no important effects on our conclusions. The finite-temperature flow stress follows by the equivalent of Eq. (4.8) as

$$\tau_y^L(T, \dot{\epsilon}) = \tau_{y0}^L \left[1 - \left(\frac{T}{T_\circ^L}\right)^{\frac{2}{3}}\right] \tag{4.15}$$

where $T_\circ^L = \Delta E_b / k \ln(\dot{\epsilon}_\circ / \dot{\epsilon})$ is the characteristic temperature for the Labusch mechanism.

At a given applied stress, the motion of the dislocation should be controlled by the mechanism having the largest energy barrier. For instance, if the energy barrier for individual solute pinning exceeds that of the collective pinning, then after the dislocation can overcome the individual barrier it can rapidly pass over the collective barrier. In terms of the flow stress at finite temperature and imposed strain rate, the controlling mechanism is therefore the one with the highest flow stress. The transition between the two regimes can thus be taken to occur when $\tau_y^F(T) = \tau_y^L(T)$, which naturally extends the zero-temperature result to finite temperatures.

For any given solute, we determine the solute concentration at which the transition occurs. At zero temperature, this critical concentration follows by setting $\tau_{y0}^F = \tau_{y0}^L$ using Eqs. (4.8) and (4.15) above to yield

$$c_\circ = 0.12 \left(\frac{w_c f_{max}}{\Delta \tilde{E}_p(w_c)} \right)^8 \left(\frac{w_c^2 f_{max}}{b^2 \Gamma} \right). \tag{4.16}$$

Comparing to the form in Eq. (4.5), something like the traditional β parameter seems to emerge but with (i) w_c in the numerator instead of w in the denominator and (ii) an additional factor that is the ratio of the Friedel maximum force f_{max} to a characteristic force quantity $\Delta \tilde{E}_p / w_c$ emerging from the collective solute energies in the Labusch-type model. The transition between the Friedel and Labusch regimes at finite temperature is calculated as the concentration at which $\tau_y^F = \tau_y^L$ at the specified temperature. Since the finite temperature yield stress for the two mechanisms scale differently with temperature, the transition concentration can be significantly different from $c_\circ$.

From the formalism above, we can see that the transition between Friedel and Labusch

mechanisms is intimately connected to the solute/dislocation interaction energies, which are in turn tied to the structure of the dislocation core. To quantitatively compute the transition concentration at any temperature requires a specific model for these interaction energies. We address this in the next section.

4.3 Effect of core structure in the Friedel-Labusch transition

Both Friedel and Labusch models require solute-dislocation interaction energies $U(x_i, y_j)$, which in turn are highly dependent on the dislocation core structure. At the atomic scale, the dislocation is delocalized to some degree over the glide plane. Additionally, in materials with sufficiently small stacking faults, the dislocation can dissociate into two partials. Both the core spreading and partial dissociation affect the characteristic forces and energies associated with both strengthening mechanisms. In order to systematically study the effect of the core structure to the transition concentration, an analytic model for a generalized dissociated dislocation core is considered.

To consider a general dislocation core, the dislocation is envisioned to have separated into two partials with separation distance d. In addition to this, each partial is delocalized around its center by a normal distribution with standard deviation σ. From this description, we generate a discrete Burgers vector distribution at positions x_k along the

slip plane $\Delta b\left(x_k\right)$ as

$$\frac{\Delta b\left(x_k\right)}{b}=\frac{\exp\left(-\frac{1}{2}\left(\frac{x_i-d/2}{\sigma}\right)^2\right)+\exp\left(-\frac{1}{2}\left(\frac{x_i+d/2}{\sigma}\right)^2\right)}{\sum_{m=-\infty}^{\infty}\left[\exp\left(-\frac{1}{2}\left(\frac{x_m-d/2}{\sigma}\right)^2\right)+\exp\left(-\frac{1}{2}\left(\frac{x_m+d/2}{\sigma}\right)^2\right)\right]} \tag{4.17}$$

Figure 4.1(a) shows $b\left(x_k\right)$ versus x for the case $d=10b$ and $\sigma=2b$. We then use the use continuum the continuun Peierls-Nabarro model to calculate the pressure field $p\left(x_i,y_j\right)$ around the dislocation. We use a discrete a discrete Peierls-Nabarro model

$$p\left(x_i,y_j\right)=\sum_{k=-\infty}^{\infty}-\mu\frac{\left(1+\nu\right)\Delta b\left(x_k\right)}{3\pi\left(1-\nu\right)}\frac{y_j}{\left(x_i-x_k\right)^2+y_j^2} \tag{4.18}$$

where μ is the shear modulus, ν is the Poisson ratio . Finally, the solute/dislocation interaction energy is given by the expression [80]

$$U\left(x_i,y_j\right)=-p\left(x_i,y_j\right)\Delta v_m, \tag{4.19}$$

where $p\left(x_i,y_j\right)$ is the pressure field due to the dislocation at position $\left(x_i,y_j\right)$ and Δv_m is the misfit volume of the solute. From these energies, the maximum resistive force $f_{max}=\max|\nabla_x U|$ due to solutes along the glide plane is calculated, which is the key material parameter in the Friedel model. These energies are also used in Eqs. (4.10)–(4.11) of our Labusch-type model.

In order to systematically ascertain the effect of the dislocation core structure to the transition concentration, d and σ is varied from 0 to $20b$ and b to $3b$ respectively. The material parameters we choose for this set of calculations correspond to Al-Mg alloys; $\mu=27.4$ GPa, $\nu=0.33$, $b=2.85$ Å, $\Gamma=0.47$ eV/Å and $\Delta v_m=5.7$ Å^3. Other metal

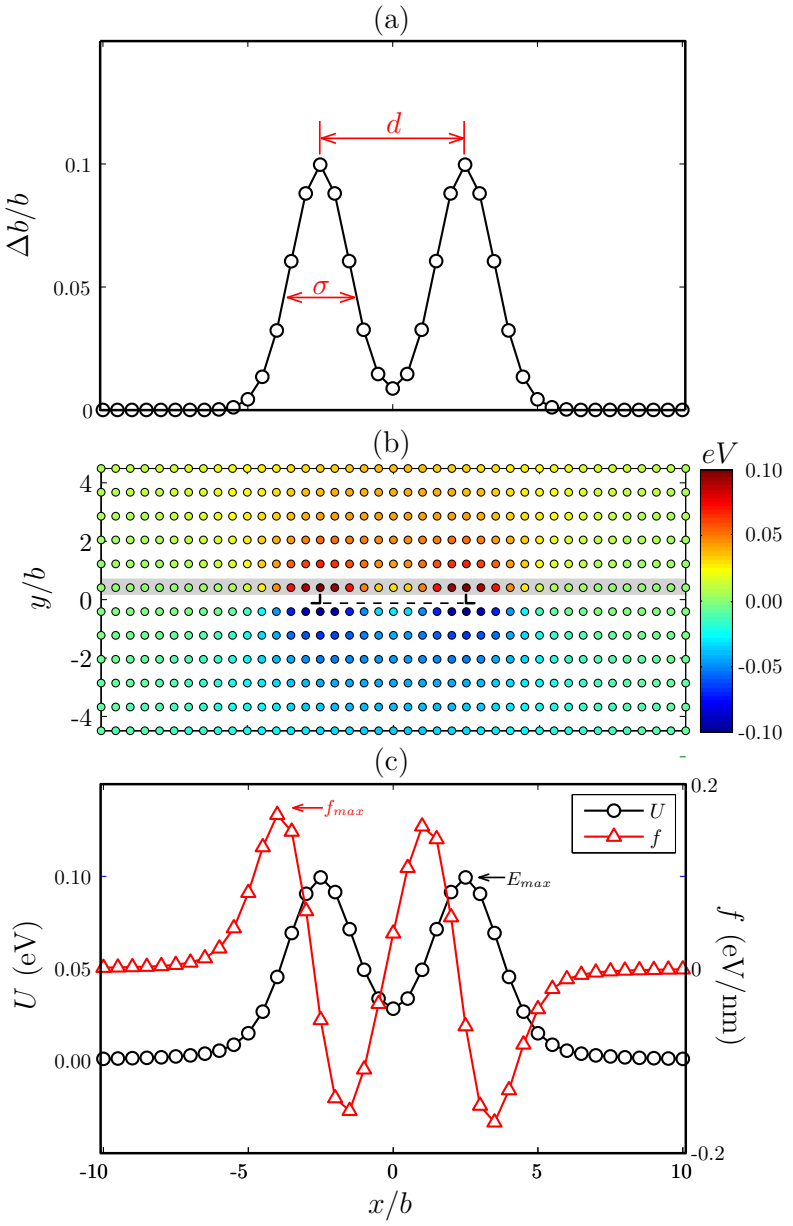

FIGURE 4.1: (a) Burgers vector distribution $\Delta b\,(x_k)$ using Eqn. (4.17) for $d = 10b$ and $\sigma = 2b$. (b) Solute dislocation interaction energy U as a function of solute position, for Mg solutes around an edge dislocation in Al; dashed line: stacking fault between two partial dislocations. (c) Solute dislocation interaction energy and resistive force f for solutes just above the glide plane (solutes highlighted in the gray bar).

systems can be considered, but this does not change the general trends observed in this analysis since the energies and forces in both the Friedel and Labusch models both scale with the elastic modulus and misfit stress, while continuum models suggest the line tension also scales with elastic modulus. Thus, when comparing Friedel and Labusch model predictions, the transition concentration versus temperature is not strongly dependent on the material properties. Where necessary, we use $\ln(\dot{\epsilon}_\circ/\dot{\epsilon}) = 20$ corresponding to typical experimental strain rates.

The locus of (c, T) points at which the transition from the Friedel mechanism to the Labusch mechanism occurs are shown in Figure 4.2, with T normalized by the concentration-independent Friedel temperature $T_\circ^F$. For an undissociated dislocation ($d = 0$), the transition concentration increases monotonically with temperature, as shown in Figures 4.2(a)–(c). The transition concentration decreases with the degree of dislocation delocalization σ for any given temperature. For dissociated dislocations $d > 0$, some core structures exhibit two minimum Labusch configurations [81]. This occurs when the interaction energies in the region between the partials are sufficiently low (i.e., when d/σ is sufficiently large). The first configuration, dominant at high T, is associated with decorrelating the interaction energies of the entire dislocation core by moving the dislocation approximately one dislocation core width away from its original position. The second configuration, dominant at low T, is associated with decorrelating the energies in the partials of the dislocation by moving about half the partial separation distance d. For cores exhibiting two Labusch minima, the transition concentration initially increases with T since both mechanisms are controlled by the partial cores, and is qualitatively similar to results for the undissociated core. However, at higher temperatures, the first

Labusch configuration becomes more favorable and is associated with much larger energy barriers (but with a smaller τ_{y0}^{L}), so that the Labusch mechanism can compete with the Friedel mechanism at these higher temperatures. As a result, the transition concentration decreases with temperature as observed in Figures 4.2(d)–(e),(g)–(i). The intermediate situation occurs when the core is dissociated into two partials but sufficiently to give two Labusch configurations (Figure 4.2(f)), the transition concentration initially decreases with T but can increase with T at higher temperatures.

Examining the actual concentrations at which the transition occurs, Figure 4.2 indicates that, with the exception of the most localized and undissociated core ($\sigma = 0; d = 0$), the transition concentration is below $c \sim 4 \times 10^{-4}$ at all temperatures. Furthermore, over wide portions of the domain of core structure and temperature, the transition concentration is below 10^{-4}. Including the more accurate high-temperature Labusch model would suppress the transition further. We also note that the Friedel model predicts zero strength at $T = T_{\circ}^{F}$, so that the actual strengths in this regime are becoming irrelevant for engineering purposes. We therefore conclude that the Friedel model has a very narrow range of applicability, limited to very localized core structures and, even within such core structures, concentrations in the range of 10^{-3} or below.

For a more realistic description of the dislocation core, the partial burgers vector $\Delta b\,(x_k)$ can be calculated directly from a numerically obtained dislocation core structure. In particular, edge basal and prism dislocations in Mg provide good examples of a dissociated and compact core, respectively, and have been studied using EAM and first principles methods [6]. The Burgers vector distribution $\Delta b\,(x_k)$ for the EAM-computed

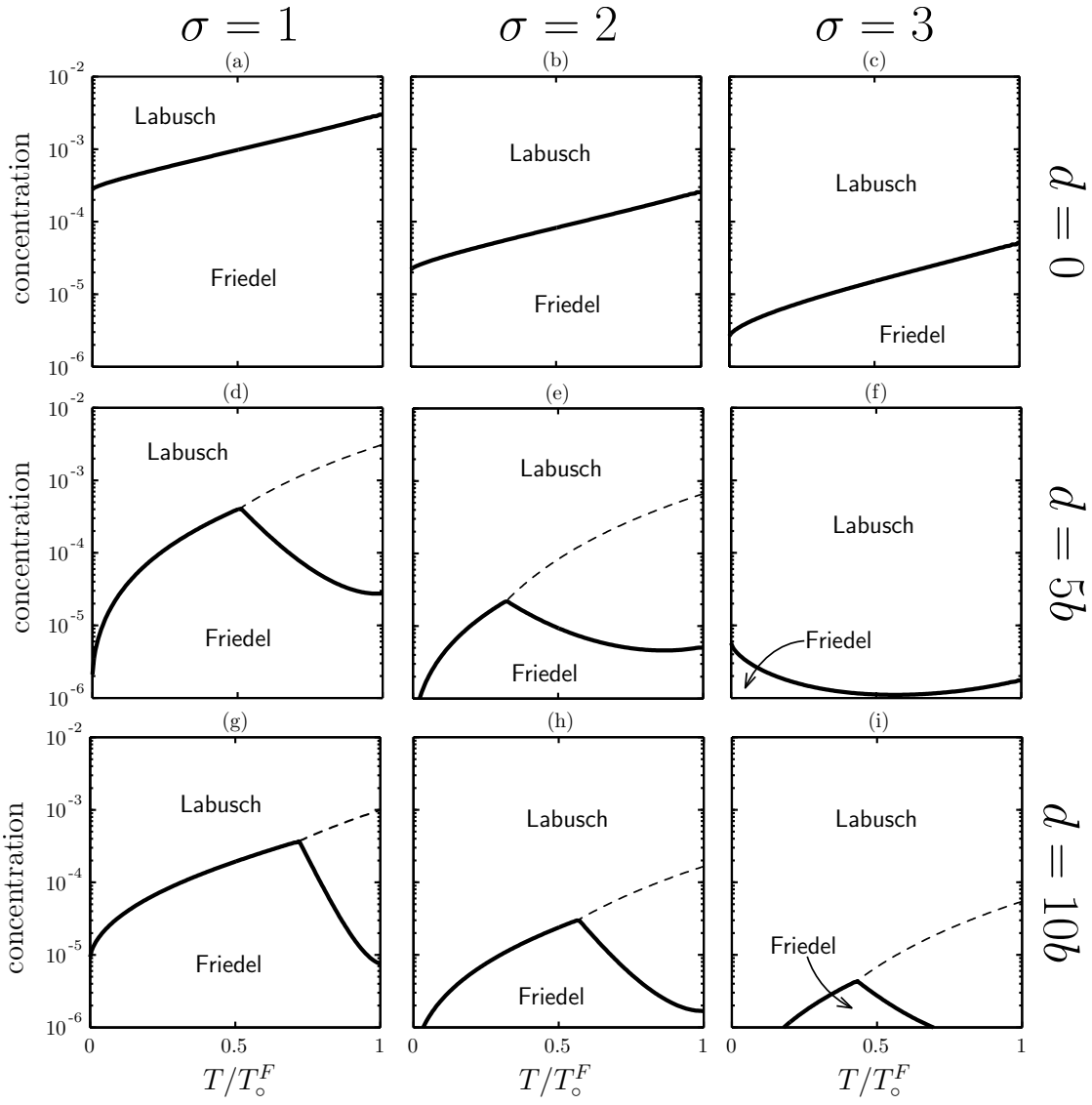

FIGURE 4.2: The Friedel-Labusch transition as a function of concentration and normalized temperature $T/T_\circ^F$ for various core structures. The interaction energies are calculated using Eqs. (4.17)–(4.19), with $d = 0$–$20b$ and $\sigma = b$–$3b$. The dashed lines indicate the transition between the two Labusch configurations.

cores, which agree well with those calculated by first principles, and the interaction energies $U(x_i, y_j)$ calculated using Eqs. (4.18) and (4.19) are shown in Figure 4.3. The anisotropy in the elastic constants of Mg are small and for simplicity we use material parameters corresponding to Mg-Al alloys in the direction of basal slip: $\mu = 19.6$ GPa, $\nu = 0.27$, $\Gamma = 0.40$ eV/Å and $\Delta v_m = -7.9$ Å^3. The predicted finite temperature Friedel-Labusch transition concentrations are shown in Figure 4.4(a). Note that using the continuum approximation for the basal interaction energies (Eq. (4.19)) yields one minimum energy configuration for the Labusch mechanism and not the two predicted using DFT-calculated energies [81]. As expected, the transition concentration for the compact prism dislocation core is higher than for the dissociated basal dislocation core. This implies that for complex crystal structures where multiple slip systems with varying core structures exist, such as in hcp, there are solute concentrations at which the Labusch mechanism controls strengthening on some slip systems (e.g. basal) while the Friedel mechanism controls strengthening on other slip systems (e.g. prism). However, the Labusch mechanism still controls strengthening for prism slip at concentrations greater than 10^{-4} over the entire range of temperatures.

From these results, it can be seen that the general trends of the finite temperature Friedel-Labusch transition can very greatly with dislocation core structure. In general, the transition can occur at concentrations much different from (and usually much lower than) the zero temperature transition concentration $c_\circ$. Moreover, with the exception of very highly localized and undissociated dislocations, the transition concentration occurs in the range $c \sim 10^{-4}$–10^{-5}, below the range of typical solute-strengthening alloy additions and where the strengthening is quite small.

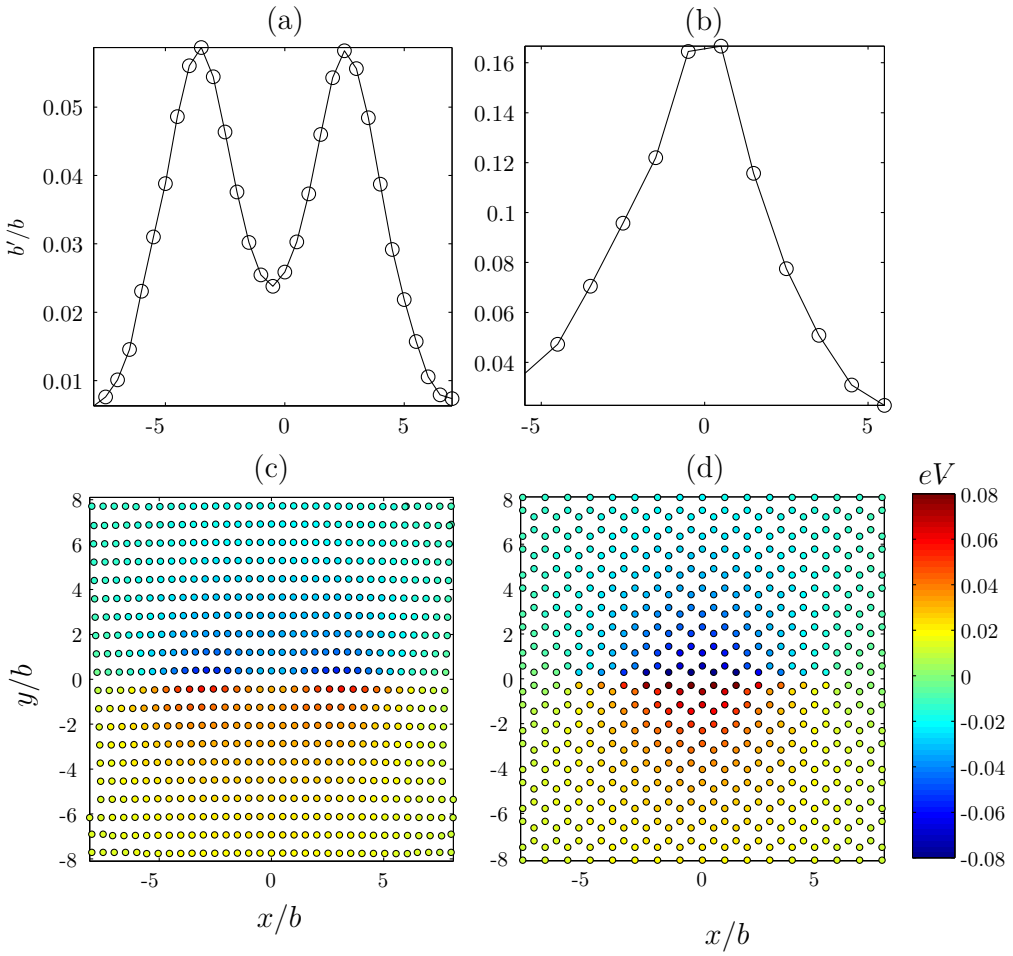

FIGURE 4.3: The partial Burgers vector $\Delta b\,(x_k)$ derived from dislocation core structures obtained from EAM calculations [6] for (a) basal and (b) prismatic dislocations in Mg. Also shown are the solute/dislocation interaction energies $U\,(x_i, y_j)$ for (c) basal and (d) prismatic dislocations using Eqs. (4.18)–(4.19) and the $\Delta b\,(x_k)$ shown in (a) and (b).

4.4 Finite temperature transition concentration using DFT energies

Continuum descriptions of the solute/dislocation interaction energies fail within the core, where the deformation and interaction energies are largest where explicit chemical effects may prevail. In previous work, we have thus used quantum-mechanical Density Functional Theory (DFT), in conjunction with a Greens Function method, to compute the

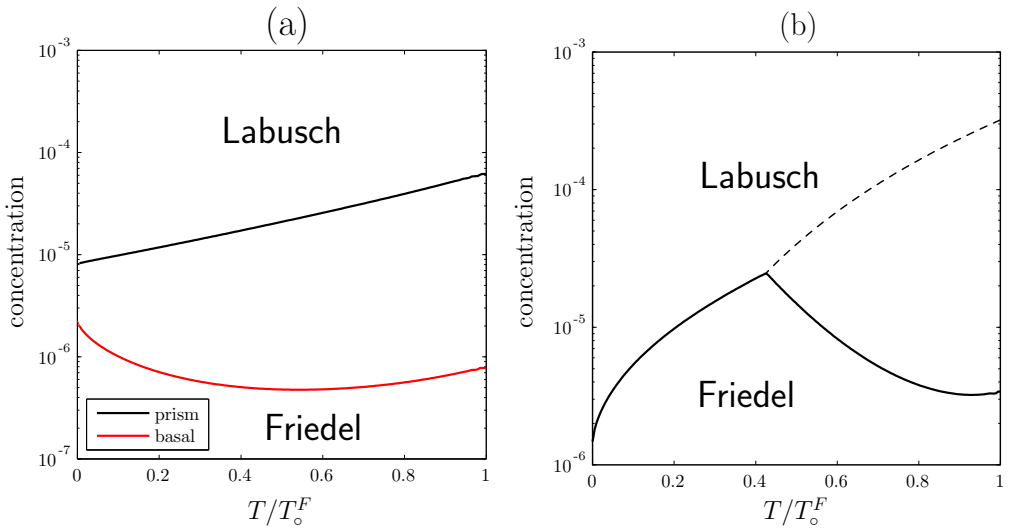

FIGURE 4.4: (a) The Friedel-Labusch transition as a function of normalized temperature $T/T_\circ^F$ for Mg-Al alloys undergoing prismatic and basal slip using the continuum approximation (Eqn. (4.19)) in conjunction with the $\Delta b\,(x_k)$ derived from EAM dislocation structures. (b) The Friedel-Labusch transition as a function of normalized temperature $T/T_\circ^F$ for Mg-Al undergoing basal slip using DFT-derived interaction energies for the core sites. The dashed line indicate the transition between the two Labusch configurations.

solute/dislocation interaction energies $U(x_i, y_j)$ in the dislocation core for Al-X alloys (X = Mg, Si, Cu, Cr, Mn and Fe) [67]. These energies also include the stacking fault in the dissociated dislocations typically of fcc metals, and are generally more accurate than the continuum approximation. Away from the core, a continuum interaction energy is calculated using the methods described in the previous section, and the results for $U(x_i, y_j)$ are consistent with the quantum calculations. Characteristic forces and energies for the Friedel and Labusch model are then calculated as described in the previous section. All quantities needed to assess the finite-temperature flow stress are shown in Table 4.1 for a range of solutes in Al.

The predicted transition concentrations for the Friedel-Labusch transition are shown in Fig. 4.5. Fig. 4.5(a) shows the locus of (c, T) transition points for Al-Mg along with contours of the associated finite temperature flow stress τ_y and with the temperature

TABLE 4.1: Friedel and Labusch force, energy, length, and/or temperature parameters, as computed for Mg, Si, Cu, Cr, Mn and Fe solutes in Al. Also shown are the zero-temperature transition concentrations $c_\circ$ and the geometrical lower limit c_{min} for the Labusch model, for each alloy.

Solute	**Friedel Parameters**		**Labusch Parameters**		**Transition Paramters**		
	$\tau_{y0}^F/c^{1/2}$ (MPa)	E_{max} (eV)	$\tau_{y0}^L/c^{2/3}$ (MPa)	$\Delta E_b/c^{1/3}$ (eV)	$c_\circ$ $(\times 10^3)$	$T_\circ^F$ (K)	c_{min} $(\times 10^5)$
Mg	147	0.11	342	4.06	6.3	63.4	1.34
Si	97	0.07	137	2.58	123.4	40.1	0.67
Cu	199	0.13	348	4.10	35.7	72.8	1.36
Cr	269	0.26	705	6.65	3.1	152.7	1.86
Mn	271	0.20	710	7.52	3.1	117.8	1.59
Fe	372	0.26	1072	8.20	1.8	152.3	2.59

normalized by $T_\circ^F$. Fig. 4.5(b) shows the locus of $(c, T_\circ^F)$ points for all the different solutes considered, where normalization by $T_\circ^F$ collapses all the data nicely. The zero temperature transition concentration $c_\circ$ is on the order of 10^{-3} for most solutes, as shown in Table 4.1. For Si, the critical concentration is larger, 10^{-1}, but the Si is the weakest alloying element among all those considered here. In all cases, the transition concentration is a strong decreasing function of temperature, dropping rapidly from $c_\circ$ to very low values 10^{-5} as T approaches $T_\circ^F$. Thus, with increasing temperature, the Labusch model rapidly become dominant over a very wide range of concentrations.

The DFT core structure corresponds reasonably closely to our simple model with $d = 5b$ and $\sigma = 3b$ (Figure 4.2(f)). Compared to the continuum approximation for the energies, the Friedel-Labusch transition occurs at higher concentrations at any given temperature, with the increase being larger at low temperatures. This difference arises because the quantum interaction energies $U(x_i, y_j)$ are generally larger in magnitude due to chemical contributions that are not included in the purely mechanical model of Eqn. (4.19). Such local increases in local interaction energy favor the strong-pinning Friedel mechanism

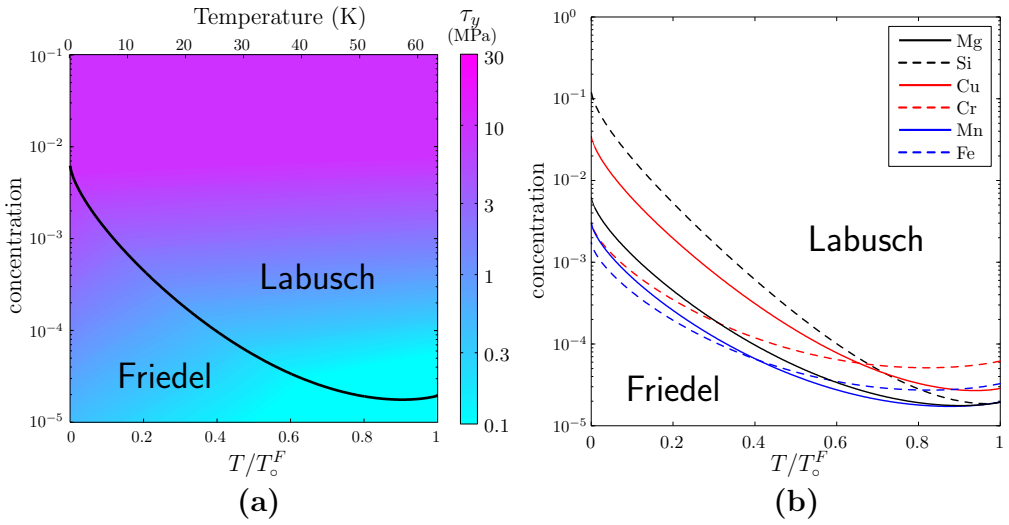

FIGURE 4.5: (a) A contour plot of the yield stress τ_y for Mg solutes in Al as a function of concentration and actual/normalized temperature. The Friedel-Labusch transition is shown as a black line. (b) The Friedel-Labusch transition as a function of concentration and normalized temperature $T/T_\circ^F$ for Mg, Si, Cu, Cr, Mn and Fe solutes in Al.

more than weak-pinning Labusch mechanism where a significant contribution ($\sim 50\%$) of the overall energy comes from solutes outside the core.

Considering actual temperature ranges, for the alloys here $T_\circ^F < 156$K (See Table 4.1). Therefore, at liquid nitrogen temperature $T = 78K$, $T/T_\circ^F > 0.5$ and the transition concentration is typically $c \sim 10^{-4}$, with corresponding strengths of $\tau_y \sim 5$ MPa or less. Temperatures relevant to many engineering applications are generally greater than $T_\circ^F$, so that the Labusch mechanism is the only applicable mechanism. It is therefore unlikely that the point pinning model is ever relevant for engineering applications of these Al-X alloys.

DFT-derived core energies for Mg-Al are available in the literature [4]. Using these energies, we calculate the relevant Friedel and Labusch parameters as we did for Al-X alloys, as well as the finite-temperature Friedel-Labusch transitition. The transition concentration as a function of normalize temperature $T/T_\circ^F$ is shown in Fig. 4.4(b). Similar to

Al-X, Mg-Al core energies near the partials are significantly larger in magnitude compared to the continuum approximation (see Figure 4.3). However, the core energies in between the partials are similar in magnitude to that of the continuum approximation. As a result, two minima are found during energy minimization, corresponding two stable dislocation configurations. The higher magnitude of the DFT core energies makes the Friedel mechanism favorable at higher conecentration compared to the continuum model but the existence of second Labusch configurations makes the Labusch model dominant at lower concentrations when $T/T_{\circ}^{F}$ is small. Thus, the Labusch model controls strengthening for concentrations larger than $\sim 10^{-5}$. We expect that materials like Cu will be similar to basal slip in hcp Mg.

4.5 Discussion and Summary

There is physical statistical lower limit to the validity of the Labusch concept that does not emerge immediately in the analysis above. Specifically, when the total actual number of solutes around the characteristic dislocation segment of length ζ_c is $\ll 1$, the statistical concept of a dislocation interacting with a random field of surrounding solutes breaks down. To calculate at what concentration this occurs, we consider the region around the dislocation within which the contributions to the interaction energy represent $\sim 80\%$ of the total solute/dislocation interaction energy. This region encompasses the first 3 atomic rows of atoms above and below the glide plane of the dislocation and over the length w_c. At concentration c, the total number N of host atoms within this dominant interaction volume is

$$N = 6\left(\frac{2w_c}{b/2}\right)\left(\frac{\zeta_{L,c}}{\sqrt{3}b}\right). \tag{4.20}$$

The average number of solutes in this region is cN and by setting $c_{min}N = 1$ and solving for the concentration we obtain the minimum concentration c_{min} for applicability of the Labusch model as

$$c_{min} = 0.24 \left(\frac{b}{4w_c} \right)^{\frac{5}{2}} \left(\frac{\Delta \tilde{E}_p \left(w_c \right)}{\Gamma w_c} \right). \tag{4.21}$$

Values of c_{min} for solutes in Al considered here are summarized in Table 4.1 and are all $\sim 10^{-5}$. If we consider the Labusch concept to fail when $c_{min}N = 10$, i.e. 10 solute atoms in the Labusch region, then this concentration would increase by $10^{2/3} \sim 30$, putting the limit in the range of 4×10^{-4}. These statistical lower limit estimates are typically close to the transition concentrations computed using the two models directly, and so do not change the conclusion that the Friedel model only prevails at very low concentrations under most conditions of interest.

Our analysis here assumes that f_{max} is determined by the greatest solute energy difference between two neighboring solute sites in the material (see Figure 4.1). It remains possible that, for some solutes, there is an additional energy barrier, and hence a larger force, in between these two locations that must be overcome if the dislocation is to glide. Such a situation might arise if the solute forms strong covalent-type bonds with the matrix material, such that the breaking of these bonds during glide determines the maximum force. Such a situation would have little or no influence on the Labusch-type model predictions but would, naturally, increase the Friedel flow stress and energy barrier. This would drive the transition between Friedel and Labusch models to higher concentrations than calculated here. Such a situation can only be assessed by further detailed first-principles calculations of the glide process, akin to measuring the unstable stacking fault energy in the presence of a solute along the glide plane. While we have

previously applied our Labusch model with success to predict the strengths in various Al-X alloys, we were not able to predict the strength of Al-Fe at the 10–50 ppm level of Fe. The anomalous case of Fe may thus fall within the situation just above, and future studies are needed to gain a quantitative understanding of dilute Fe in Al.

Finally, our conclusion about the broad irrelevance of the Friedel model for solute strengthening is generally supported by experimental measurements of the activation volume $V = -\partial \Delta E(\tau)/\partial \tau$. Many solute-strengthened alloys exhibit stress equivalence [1, 2, 16, 21, 82], wherein the relationship between the activation volume V and the finite temperature yield stress τ_y is invariant to the type of solute in a given host material. It is well-known that the Friedel model does not show stress equivalence while the Labusch model does [16, 67]. For clarity, Figure 4.6 shows the predicted activation volumes versus finite temperature flow stress for all the Al-X alloys considered here over a range of concentrations at $T = 78$ K. While the Friedel model predicts the experimentally observed scaling of $V \sim \tau_y^{-1}$ [20], the prefactor in the Friedel scaling is solute-dependent and does not exhibit stress equivalence. Furthermore, at typical experimental conditions at which stress equivalence is observed (that is, $T \geq 78$ K), the Friedel model predicts no strengthening for Mg, Si and Cu solutes in Al, as shown in Figure 4.6. On the other hand, the Labusch-type model gives a smaller power scaling of $\sim 2/3$ but is consistent with stress equivalence [67]. Small deviations on the curve is due to small difference in w_c between the solutes, which vary very slightly between all solute types. Experimental observations of stress equivalence down to solute concentrations at the level of 10^{-4}, and at low temperatures [16], suggest that the Labusch model applies at such low concentrations, consistent with our analyses here.

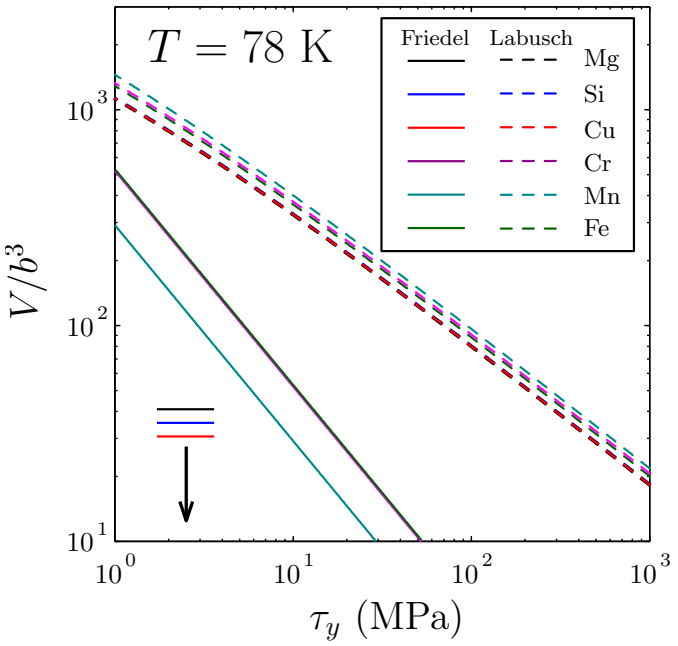

FIGURE 4.6: The normalized activation volume V/b^3 as a function of finite temperature yield stress τ_y for Mg, Si, Cu, Cr, Mn and Fe at $T = 78$ K. Note that the Friedel model predicts that $V = 0$ for Mg, Si and Cu solutes.

In summary, the finite temperature transition between strong-pinning Friedel mechanism and the weak-pinning Labusch mechanism has been studied by evaluating the finite temperature yield stress as predicted by the Friedel model and our new Labusch-type model. A parametric study using a range of dislocation core structure showed that the Labusch model controls strengthening for most core structures and concentrations above 10^{-4}, over a wide range of temperature, but with the transition concentration increasing for very localized cores. The transition was also studied using DFT-calculated solute/dislocation interaction energies for Al-X (X = Mg, Si, Cu, Cr, Mn and Fe) and Mg-Al (basal) alloys. In all cases, the transition concentration are found to be a strong function of temperatures, with the Labusch-type model controlling the strength at most temperatures ($T > 78K$) and solute concentrations $c > 10^{-4}$ of relevance to engineered

alloys. This conclusion is contrary to a conclusion obtained by considering only the zero-temperature limit, where the Labusch model dominates only for $c \sim 2 \times 10^{-3}$ or higher. We conclude that applicability of the Friedel model is very limited in core structure, temperature, and solute concentration, so that use of the Labusch-type model is more appropriate for most materials and engineering applications.

Chapter 5

Summary and Conclusions

In the first part of this dissertation, we developed a new Labusch-type model for solute strengthening in general substitutional alloys that addresses some of the shortcomings inherent in previous weak-pinning models. The major feature of the model is that it takes into account the correlations between solute/dislocation interaction energies as the dislocation moves along the glide plane. By considering these correlations, the divergent nature of the dislocation field is taken into account without the need to introduce arbitrary cut-offs in the interaction energy. The resulting model is parameter-free, gives predictions for finite temperature yield stresses and is applicable to multi-solute alloys.

The model takes as input the solute/dislocation interaction energy of a solute around the dislocation as a function of solute position. In positions immediately adjacent to the stacking fault, continuum elasticity breaks down and chemical effects are more significant. To obtain accurate energies on those positions, we use the flexible Greens Functions Flexible Boundary method is used in conjunction with state-of-the-art Density

Functional Theory calculations. This methodology is used to compute the interaction energies of Al-X alloys (X = Mg, Si, Cu, Cr, Mn and Fe). Using the DFT-computed energies and the new parameter-free model, quantitative predictions of finite temperature yield stresses are made for several Al-based alloys characterized in experimental studies. The predictions are accurate for most of the solutes considered. The notable exceptions to this are for alloys containing Fe solutes, wherein the experiments show that alloys containing Fe solutes with $c \sim 10^{-6}$ have yield strengths on the order of 10 MPa. While this result is several orders of magnitude higher than what the model predicts, the experimental yield stresses for Al-Fe alloys obey the same scaling behavior as what the model predicts (that is, $\tau_y \propto c^{2/3}$). The model is used to back calculate the parameters necessary to obtain the experimental results. When the anomalous behavior of Fe solutes is taken into account, the predictions made by the model are accurate for all the solutes types as well as all temperature ranges. We also rigorously showed that Basinski's "stress equivalency principle" is obeyed by the model.

We then applied the model without modification to basal slip in Mg-Al alloys using DFT-obtrained interaction energies existing in the literature [4]. Due to the large partial separation of basal edge dislocations in Mg, two stable configurations are found. The first configuration, dominant at high τ/low T conditions, is associated to decorrelating the solutes within the partials of the dislocation while the second, dominant at low τ/high T conditions, is associated with decorrelating the solutes in the far-field. The existence of these two configurations is confirmed by stochastic analysis. Due to the two configurations, the dependence of $\tau_y(T)$ versus T in Mg-Al undergoing basal slip have features not found in Al-X alloys. In particular, the temperature dependence of

the finite temperature yield stress abruptly changes as the dislocation goes from one regime to another. This behavior explains the experimentally observed "plateau stress" without the need to invoke ambiguous strengthening mechanisms. Predictions are made for three Mg-Al alloys and compared with experiments. These predictions are accurate for all solute concentrations over all the temperature range.

Finally, we studied the effect of temperature to the transition between the strong-pinning regime (represented by the Friedel Model) and the weak-pinning regime (represented by the Labusch model). It was found the transition concentration at finite temperatures can be significantly different from the transition concentration at zero temperature. The behavior of the transition concentration with temperature is a strong function of dislocation core structure, with compact cores favoring strong-pinning while dissociated/delocalized cores favors weak-pinning. Additionally, using the DFT-obtained interaction energies, the transition concentration is on the order of 10^{-5} or less when $T > 78$ K for both Al-X alloys and Mg-Al. The strengthening at these concentrations are on the order of the Peierls stress. It is therefore unlikely that the strong-pinning model is applicable at concentrations and temperatures relevant to engineering applications for these alloys.

Bibliography

[1] B J Diak and S Saimoto. The determination of solute clusters in dilute aluminum alloys using strain rate sensitivity. *Materials Science and Engineering A-Structural Materials Properties*, 234:1019–1022, 1997.

[2] B J Diak, K R Upadhyaya, and S Saimoto. Characterization of thermodynamic response by materials testing. *Progress in Materials Science*, 43(4):223–363, 1998.

[3] B J Diak. *Private communication*, 2011.

[4] J A Yasi, L G Hector Jr., and D R Trinkle. First principles data for solid-solution strengthening in magnesium: from geometry and chemistry to properties. *Acta Materialia*, 58:5704–5713, 2010.

[5] A Akhtar and E. Teghtsoonian. Substitutional solute hardening of magnesium single crystals. *Philosophical Magazine*, 25(4):897–916, 1972.

[6] J A Yasi, T Nogaret, D R Trinkle, Y Qi, L G Hector Jr., and W A Curtin. Basal and prism dislocation cores in magnesium: comparison of first-principles and embedded-atom-potential methods predictions. *Modeling and Simulations in Materials Science and Engineering*, 17(5):055012, 1–13, 2009.

[7] R L Fleischer. Solution hardening. *Acta Metallurgica*, 9(11):996–1000, 1961.

[8] J Friedel. *Les Dislocations*, page 205. Gauthier-Villars, Paris, 1956.

[9] R L Fleischer. Substitutional solution hardening. *Acta Metallurgica*, 11:203–209, 1963.

[10] M Zaiser. Dislocation motion in a random solid solution. *Philosophical Magazine A*, 82(15):2869–2883, 2002.

[11] P Haasen. *Physical Metallurgy*. Cambridge University Press, USA, 1996.

[12] U F Kocks, A S Argon, and M F Ashby. Thermodynamics and kinetics of slip. *Progress in Materials Science*, 19:1–281, 1975.

[13] R Labusch. A statistical theory of solid solution hardening. *Physica Status Solidi B*, 41(2):659–669, 1970.

[14] N F Mott and F R N Nabarro. Dislocation theory and transient creep. *Physical Society Bristol Conference Report*, pages 1–19, 1948.

[15] R Labusch. Statistical theories of solid-solution hardening. *Acta Metallurgica*, 20: 917–927, 1972.

[16] F R N Nabarro. Equivalence in the theory of solution hardening. *Proceedings of the Royal Society of London, Series A*, 381(1781):285–292, 1985.

[17] T H Wille, W Gieseke, and Schwink C H. Quantitative analysis of solution hardening in selected copper alloys. *Acta Metallurgica*, 35(11):2697–2693, 1987.

[18] W E Nixon and J W Mitchell. The yield stress of single crystals of α-phase copper-aluminium alloys. *Proceedings of the Royal Society of London, Series A*, 376(1766): 343–59, 1981.

[19] R B Schwarz and R Labusch. Dynamic simulation of solution hardening. *Journal of Applied Physics*, 49(10):5174–5187, 1978.

[20] D Caillard and J L Martin. *Thermally Activated Mechanisms in Crystal Plasticity.* Pergamon, 2003.

[21] A S Argon. *Strengthening Mechanisms in Crystal Plasticity.* Oxford University Press, USA, 2007.

[22] R J Arsenault and S Li. Computer simulation of thermally activated dislcocation motion: Part iii. in fcc solid solutions. *Metallurgical Transactions A*, 20A:1429–1436, 1989.

[23] R B Schwartz and R Labusch. Dynamic simulation of solution hardening. *Journal of Applied Physics*, 49(10):5174–5186, 1978.

[24] M Lebyodkin, Y Brechet, Y Estrin, and L Kubin. Statistical behavior and strain localization patterns in the portevin–le chatelier effect. *Acta Materialia*, 44(11): 4531–4541, 1996.

[25] S Zapperi and M Zaiser. Depinning of a dislocation: the influence of long-range interactions. *Materials Science and Engineering A*, 309–310:348–351, 2001.

[26] D L Olmsted, L G Hector Jr., and W A Curtin. Molecular dynamics study of solute strengthening in Al/Mg alloys. *Journal of The Mechanics and Physics of Solids*, 54 (8):1763–1788, 2006.

[27] E. Rodary, D. Rodney, L. Proville, Y. Bréchet, and G. Martin. Dislocation glide in model Ni (Al) solid solutions by molecular dynamics. *Physical Review B*, 70(5): 054111,1–11, 2004.

[28] K Tapasa, D J Bacon, and Y N Osetsky. Computer simulation of dislocation-solute interaction in dilute FeCu alloys. *Modelling and Simulation in Materials Science and Engineering*, 14(7):1153–1166, 2006.

[29] K. Tapasa, D J Bacon, and Yu N Osetsky. Simulation of dislocation glide in dilute Fe-Cu alloys. *Materials Science and Engineering A*, 400-401:109–113, 2005.

[30] L Proville and S Patinet. Atomic-scale models for hardening in fcc solid solutions. *Physical Review B*, 82(5):054115,1–19, 2010.

[31] S. Patinet and L. Proville. Depinning transition for a screw dislocation in a model solid solution. *Physical Review B*, 78(10):104109,1–9, 2008.

[32] D Warner. Private communications. 2011.

[33] D R Trinkle and C Woodward. The chemistry of deformation: How solutes soften pure metals. *Science*, 310(5754):pp. 1665–1667, 2005.

[34] J Zander, R Sandstrom, and L Vitos. Modelling mechanical properties from non-hardenable aluminum alloys. *Computational Materials Science*, 41:86–95, 2007.

[35] J Zander and R Sandstrom. One parameter model for strength properties of hard-enable aluminum alloys. *Materials and Design*, 29:1540–1548, 2008.

[36] R.L. Fleischer. Substitutional solution hardening of copper. *Acta Metallurgica*, 14 (12):1867–1868, 1966.

[37] G P M Leyson, W A Curtin, L G Hector Jr., and C F Woodward. Quantitative prediction of solute strengthening in aluminum alloys. *Nature Materials*, 9:750–755, 2010.

[38] G Kresse and J Hafner. Ab initio molecular dynamics for liquid metals. *Physical Review B*, 47(1):558–561, 1993.

[39] G Kresse and J Furthmuller. Efficient iterative schemes for ab initio total-energy calculations using a plane-wave basis set. *Physical Review B*, 54(16):11169–11186, 1996.

[40] D Vanderbilt. Soft self-consistent pseudopotentials in a generalized eigenvalue formalism. *Physical Review B*, 41(11):7892–7895, 1990.

[41] J P Perdew and Y Wang. Accurate and simple analytic representation of the electron-gas correlation-energy. *Physical Review B*, 45(23):13244–13249, 1992.

[42] J P Perdew and Y Wang. Pair-distribution function and its coupling-constant average for the spin-polarized electron-gas. *Physical Review B*, 46(20):12947–12954, 1992.

[43] C Woodward, D R Trinkle, L G Hector Jr., and D L Olmsted. Prediction of dislocation cores in aluminum from density functional theory. *Physical Review Letters*, 100(4):045507,1–4, 2008.

[44] HJ Monkhorst and JD Pack. Special points for brillouin-zone integrations. *Physical Review B*, 13(12):5188–5192, 1976.

[45] M Methfessel and A T Paxton. High-precision sampling for brillouin-zone integration in metals. *Physical Review B*, 40(6):3616–3621, 1989.

[46] C Woodward and S I Rao. Flexible ab initio boundary conditions: Simulating isolated dislocations in bcc Mo and Ta. *Physical Review Letters*, 88(21):216402,1–4, 2002.

[47] S Vannarat, M H F Sluiter, and Y Kawazoe. First-principles study of solute-dislocation interaction in aluminum-rich alloys. *Physical Review B*, 64:224203,1–8, 2001.

[48] Z S Basinski, R A Foxall, and R Pascual. Stress equivalence of solution hardening. *Scripta Metallurgica*, 6(9):807–814, 1972.

[49] F R N Nabarro. Thermally activated dislocation glide in moderately concentrated solid solutions. *Philosophical Magazine B*, 52(3):785–793, 1985.

[50] Y Dong, J Song, and W A Curtin. unpublished.

[51] B L Mordike and T Ebert. Magnesium: Properties applications potential. *Materials Science and Engineering: A*, 302(1):37–45, 2001.

[52] M F Horstemeyer and P Wang. Cradle-to-grave simulation-based design incorporating multiscale microstructure-property modeling: Reinvigorating design with science. *Journal of Computer-aided Materials Design*, 10(1):13–34, 2003.

[53] E Aghiona, B Bronfina, and D Eliezerb. The role of the magnesium industry in protecting the environment. *Journal of Materials Processing Technology*, 117(3): 381–385, 2001.

[54] D J Bacon and M H Liang. Computer-simulation of dislocation cores in hcp metals. 1. interatomic potentials and stacking fault stability. *Philosophical Magazine A*, 53 (2):163–179, 1986.

[55] M H Liang and D J Bacon. Computer-simulation of dislocation cores in hcp metals. 2. core structure in unstressed crystals. *Philosophical Magazine A*, 53(2):181–204, 1986.

[56] M H Liang and D J Bacon. Computer-simulation of dislocation cores in hcp metals. 2. effect of applied shear strain. *Philosophical Magazine A*, 53(2):205–220, 1986.

[57] J R Morris, K M Ho, K Y Chen, G Rengarajan, and M H Yoo. Large-scale atomistic study of core structures and energetics of $\langle c+a\rangle\{11\bar{2}2\}$ dislocations in hexagonal close packed metals. *Modelling and Simulation in Materials Science and Engineering*, 8(1):25–35, 2000.

[58] S Ando, T Gotoh, and H Tonda. Molecular dynamics simulation of $\langle c+a\rangle$ dislocation core structure in hexagonal-close-packed metals. *Metallurgical and Materials Transactions A*, 33(13):823–829, 2002.

[59] S Groh, E B Marin, M F Horstemeyer, and D J Bammann. Dislocation motion in magnesium: a study by molecular statics and molecular dynamics. *Modelling and Simulation in Materials Science and Engineering*, 17(7):075009,1–15, 2009.

[60] T Nogaret, W A Curtin, J A Yasi, L G Hector, and D R Trinkle. Atomistic study of edge and screw $\langle c+a\rangle$ dislocations in magnesium. *Acta Materialia*, 58(13): 4332–4343, 2010.

[61] J Wang, J P Hirth, and C N Tomé. Twinning nucleation mechanisms in hexagonal-close-packed crystals. *Acta Materialia*, 57(18):5521–5530, 2009.

[62] B Li and E Ma. Zonal dislocations mediating twinning in magnesium. *Acta Materialia*, 57(6):1734–1743, 2009.

[63] J Wang, I J Beyerlein, and C N Tomé. An atomic and probabilistic perspective on twin nucleation in magnesium. *Scripta Materialia*, 63(7):741–746, 2010.

[64] Y Wang, L Q Chen, Z K Liu, and S N Mathaudhu. First-principles calculations of twin-boundary and stacking-fault energies in magnesium. *Scripta Materialia*, 62 (9):646–649, 2010.

[65] R Wang, S F Wang, X Z Wu, and Q Y Wei. First-principles determination of dislocation properties in magnesium based on the improved peierls-nabarro equation. *Physica Scripta*, 81(6):065601, 1–6, 2010.

[66] I Shin and E A Carter. Orbital-free density functional theory simulations of dislocations in magnesium. *Modelling in Materials Science and Engineering*, 20(1): 015006, 1–23, 2012.

[67] Solute strengthening from first-principles and applications to aluminum alloys. *Acta Materialia*, 60:3873–3884, 2012.

[68] A Akhtar and E. Teghtsoonian. Solid solution strengthening in magnesium single crystal - alloying behaviour in basal slip. *Acta Metallurgica*, 17(11):1339–1349, 1969.

[69] P Jax, P Kratochvil, and P Haasen. Solid solution hardening in gold and other fcc single crystals. *Acta Metallurgica*, 18(2):237–245, 1970.

[70] O Boser. Temperature independent plateau stress of solid-solution crystals. *Metallurgical Transactions*, 3(4):843–849, 1972.

[71] H Traub, H Neuhausser, and C Schwink. Investigations of yield region of concentrated Cu-Ge and Cu-Zn single crytals. 1. critical resolved shear-stress, slip plane formation and true strain rate. *Acta Metallurgica*, 25(4):437–446, 1977.

[72] T Wille and C Schwink. On the plastic behavior of concentrated Cu-Mn single crystals. *Scripta Metallurgica*, 14(8):923–928, 1980.

[73] H Wendt and R Wagner. Mechanical properties of Cu-Fe alloys in the transition from solid-solution to precipitation hardening. *Acta Metallurgica*, 30(8):1561–1570, 1982.

[74] T Wille and C Schwink. Precision measurements of critical resolved shear-stress in CuMn alloys. *Acta Metallurgica*, 34(6):1059–1069, 1986.

[75] M Z Butt and P Feltham. Solid solution hardening. *Journal of Materials Science*, 28(10):2557–2576, 1993.

[76] K Marukawa. A new model of solution hardening in fcc metals based on the interaction with plural obstacles. *Philosophical Magazine*, 87(26):4027–4046, 2007.

[77] P Kratochvil and E Neradova. Solid-solution hardening in some copper base alloys. *Czechoslovak Journal of Physics B*, 21(12):1273–1279, 1971.

[78] Y Chino, M Kado, T Ueda, and M Mabuchi. Solid solution strengthening for Mg-3.0 mass pct (2.71 at. pct)Al and Mg-0.06 mass pct (0.036 at. pct)Ca alloys. *Metallurgical and Materials Transactions A*, 42A(7):1965–1973, 2011.

[79] R Labusch, G Grange, J Ahearn, and P Haasen. Rate processes in plastic deformation of materials. page 26, Cleveland, OH, 1975. American Society for Metals.

[80] J P Hirth and J Lothe. *Theory of Dislocations*. Krieger Publishing Company, Florida, USA, second edition, 1982.

[81] G P M Leyson, L G Hector Jr, and W A Curtin. First-principles prediction of yield stress for basal slip in Mg-Al alloys. *Acta Materialia*, (in press), 2012.

[82] M Z Butt and P Feltham. Solid-solution hardening. *Journal of Materials Science*, 28(10):2557–2576, 1993.